



# Mid-infrared Studies of Dusty Sources in the Galactic Center

Harshitha K. Bhat<sup>1,2</sup> , Nadeen B. Sabha<sup>1,3</sup> , Michal Zajaček<sup>1,4</sup> , Andreas Eckart<sup>1,2</sup> , Rainer Schödel<sup>5</sup> ,  
S. Elahé Hosseini<sup>1,2</sup> , Florian Peißker<sup>1</sup> , and Anton Zensus<sup>2</sup>

<sup>1</sup> I. Physikalisches Institut der Universität zu Köln, Zùlpicher Str. 77, D-50937 Köln, Germany

<sup>2</sup> Max-Planck-Institut für Radioastronomie (MPIfR), Auf dem Hügel 69, D-53121 Bonn, Germany

<sup>3</sup> Institut für Astro- und Teilchenphysik, Universität Innsbruck, Technikerstrasse 25/8, A-6929 Innsbruck, Austria

<sup>4</sup> Department of Theoretical Physics and Astrophysics, Faculty of Science, Masaryk University, Kotlářská 2, 611 37 Brno, Czech Republic

<sup>5</sup> Instituto de Astrofísica de Andalucía (CSIC), Glorieta de la Astronomía s/n, E-18008 Granada, Spain

Received 2021 November 29; revised 2022 March 21; accepted 2022 March 23; published 2022 April 27

## Abstract

Mid-infrared (MIR) images of the Galactic center show extended gas and dust features along with bright infrared sources (IRS). Some of these dust features are a part of ionized clumpy streamers orbiting Sgr A\*, known as the mini-spiral. We present their proper motions over a 12 yr time period and report their flux densities in *N*-band filters and derive their spectral indices. The observations were carried out by VISIR at the ESO's Very Large Telescope. High-pass filtering led to the detection of several resolved filaments and clumps along the mini-spiral. Each source was fit by a 2D Gaussian profile to determine the offsets and aperture sizes. We perform aperture photometry to extract fluxes in two different bands. We present the proper motions of the largest consistent set of resolved and reliably determined sources. In addition to stellar orbital motions, we identify a stream-like motion of extended clumps along the mini-spiral. We also detect MIR counterparts of the radio tail components of the IRS 7 source. They show a clear kinematical deviation with respect to the star. They likely represent Kelvin–Helmholtz instabilities formed downstream in the shocked stellar wind. We also analyze the shape and orientation of the extended late-type IRS 3 star that is consistent with the Atacama Large Millimeter/submillimeter Array submillimeter detection of the source. Its puffed-up envelope with a radius of  $\sim 2 \times 10^6 R_{\odot}$  could be the result of the red-giant collision with a nuclear jet, which was followed by tidal prolongation along the orbit.

*Unified Astronomy Thesaurus concepts:* Galactic center (565); Infrared photometry (792); Galaxy kinematics (602)

## 1. Introduction

High-angular-resolution observations of the vicinity of the compact radio source Sgr A\* in the Galactic center (GC), which is associated with the supermassive black hole (SMBH; Eckart et al. 2002; Genzel et al. 2010; Falcke & Markoff 2013; Eckart et al. 2017), showed the presence of a ring of dense clumpy molecular and neutral gas and warm dust, called the circum-nuclear disk (CND), extending from  $\sim 1.5$  to  $\sim 7$  pc (Vollmer et al. 2004; Christopher et al. 2005; Mills et al. 2013; Hsieh et al. 2021). The CND surrounds an ionized central cavity which has a much lower mean gas density within  $\sim 1$ – $1.5$  pc radius with a total mass of  $\sim 60 M_{\odot}$  (Lo & Claussen 1983; Blank et al. 2016). At the Bondi radius,  $r_B \sim 0.14(k_B T / 1.3 \text{ keV})^{-1} \text{ pc}$ , the mean electron number density is  $n_e = 26 f_V^{-1/2} \text{ cm}^{-3}$  (Baganoff et al. 2003), where  $f_V$  is the filling factor of 1.3 keV plasma, while the CND density reaches  $\sim 10^6$ – $10^8 \text{ cm}^{-3}$  in molecular cores (Jackson et al. 1993; Shukla et al. 2004; Christopher et al. 2005). Mossoux & Eckart (2018) found a depression in the X-ray surface brightness at the position of the CND, which could be attributed to the CND acting as a barrier for the hot and diluted plasma in the central cavity. A system of orbiting ionized clumpy streamers and gas filaments extending inwards from the inner edge of the CND is denoted as the mini-spiral (Lo & Claussen 1983; Nitschai et al. 2020, and references therein). The western arc of the mini-spiral appears to have a circular orbit similar to the neutral gas in the CND. However, the northern and

the eastern arms penetrate deep into the ionized cavity on eccentric orbits and reach up to a few arcseconds from Sgr A\*, possibly colliding in the Bar region (Becklin et al. 1982; Jackson et al. 1993; Christopher et al. 2005; Zhao et al. 2009).

There have been several studies on the kinematics of the mini-spiral. Vollmer & Duschl (2000) derived a 3D kinematic model of gas streams that describes the bulk motion of the mini-spiral in three different planes based on a data cube of the [Ne II] line ( $12.8 \mu\text{m}$ ), with the main plane coinciding with the inner rim of the CND. Paumard et al. (2006) performed a kinematic study and showed that the northern arm consists of a weak continuous surface that is drawn into a narrow stream near Sgr A\*. Using *L'*-band data ( $3.8 \mu\text{m}$ ), Mužić et al. (2007) provided proper motions of a number of thin dusty filaments along the mini-spiral and considered a central, partially collimated outflow as the possible explanation for their formation and motion along the mini-spiral, with some deviations from a purely Keplerian rotation. Based on radio observations using the H92 $\alpha$  and H30 $\alpha$  lines, Zhao et al. (2009) and Zhao et al. (2010) determined the 3D velocity field of the mini-spiral. The ionized streamers can dynamically be modeled as a system of three bundles of quasi-Keplerian orbits in the potential dominated by the central mass of  $\lesssim 10^7 M_{\odot}$ , i.e., dominated by Sgr A\* (Zhao et al. 2009, 2010). The orbital planes of the northern arm and the western arc are nearly coplanar, while the eastern arm plane is perpendicular to them.

In the central parsec, there is a nuclear stellar cluster (NSC) that consists predominantly of the nearly spherical old cluster of late-type stars as well as the cusp of  $\sim 100$  massive young OB/Wolf–Rayet (WR) stars that supply about  $3 \times 10^{-3} M_{\odot} \text{ yr}^{-1}$  in the form of stellar winds (Najarro et al. 1997; Moultaqa et al. 2004;

Schödel et al. 2014). However, less than 1% of the Bondi accretion rate is accreted by Sgr A\* (Bower et al. 2003; Marrone et al. 2006; Wang et al. 2013). Blandford & Begelman (1999) proposed a solution for the low accretion rate with the adiabatic inflow-outflow model, in which most of the gas that is accreted has positive energy and is lost through winds and only a small fraction is accreted onto the SMBH. Observational evidence for the outflow first emerged with the detection of the “mini-cavity” region on radio maps by Yusef-Zadeh et al. (1990). The detection of a strong [Fe III] bubble surrounding Sgr A\* (Eckart et al. 1992; Lutz et al. 1993) has led to the conclusion that the fast wind originating within the central few arcseconds blows into the orbiting streamers creating an expanding gas bubble. This has also been supported by Peißker et al. (2020b), who found that some identified dusty sources located to the west within the S cluster exhibit Doppler-shifted [Fe III] multiplet lines that could be excited by the collimated wind outflowing in their direction toward the mini-cavity. The extended region of low excitation centered on Sgr A\* (Schödel et al. 2007) and the mass-losing envelope, along with the extended tail of IRS 7 (Yusef-Zadeh & Melia 1992), could also be influenced by a strong central wind coming from the central few arcseconds. Closer to Sgr A\*, the orientation of infrared-excess, comet-shaped sources X7, X3, and X8 suggests the presence of a fast, collimated outflow that originates in the Sgr A\* accretion flow or in the collective wind of OB/WR stars (Mužić et al. 2010; Peißker et al. 2019; Yusef-Zadeh et al. 2020; Peißker et al. 2021). The nuclear outflow that nearly balances the inflow is also consistent with the flat number density profile of hot plasma,  $n_e \propto r^{-0.5}$ , inside the Bondi radius, as inferred from the analysis of the X-ray bremsstrahlung surface-density profile (Wang et al. 2013). In a broader context, the past active jet of Sgr A\* could have contributed to the depletion of bright red giants in the GC due to the intense stripping and truncation of their extended envelopes (Zajaček et al. 2020a, 2020b; Karas et al. 2021).

To fully understand the dynamics of these processes, it becomes important to get proper motions or tangential velocities of the various parts of the CNB as well as the mini-spiral. The dynamics as well as the physical properties of gaseous-dusty structures within the sphere of the gravitational influence of Sgr A\* are crucial for the understanding of the mass and the momentum transport from larger to smaller scales all the way to Sgr A\*.

In this work, we analyze mid-infrared (MIR) images of the central parsec at two wavelengths in the *N* band, the 8.59  $\mu\text{m}$  (PAH1 filter) and the 13.04  $\mu\text{m}$  (Ne II\_2 filter), over the course of 12 yr. This allows us to study the proper motions of infrared-excess sources of the NSC as well as of identified extended objects in the mini-spiral region. The photometric information at two wavelengths enables us to infer the spectral indices that in turn shed light on the properties of the identified sources. We manage to identify MIR components associated with the circumstellar material of two late-type stars, IRS 7 and IRS 3, which manifest their interaction with the circumnuclear medium.

The paper is structured as follows. In Section 2, we describe the data set used and the imaging tools that were applied. Subsequently, in Section 3, we describe the main results of the analysis, including the MIR differential map, tangential velocities, and the photometry, including spectral indices. In particular, we focus on the identification of the MIR components of IRS 7, the extended circumstellar structure of

**Table 1**  
Details of the Observed VISIR Images at Each Epoch

Year	Pixel Scale	FOV of a Single Image
2006	0''075	19''2 $\times$ 19''2
2007	0''075	19''2 $\times$ 19''2
2010	0''127	32''5 $\times$ 32''5
2016	0''045	38''0 $\times$ 38''0
2018	0''045	38''0 $\times$ 38''0

IRS 3, and the general characteristics of the identified dusty sources. We discuss the results in Section 4, and subsequently conclude with Section 5.

## 2. Data and Observations

### 2.1. VISIR

Observations were carried out at the ESO’s Very Large Telescope (VLT, UT3) using the VLT Imager and Spectrometer for the mid-InfraRed (VISIR) at five different epochs covering a total time from 2006 to 2018 in the *N*-band PAH1 (8.59  $\mu\text{m}$ ) and Ne II\_2 (13.04  $\mu\text{m}$ ). Depending on the atmospheric conditions, VISIR provides 0''25–0''4 angular resolution imaging with high sensitivity. The data used here were obtained as a part of a larger survey (N. B. Sabha et al. 2022, in preparation). The field of view (FOV) and spatial pixel size at each epoch is listed in Table 1. To increase the signal-to-noise ratio (S/N), jittered images with different offsets were added to create a mosaic with a slightly larger FOV. To reduce the bright and varying MIR background, differential observations with the chop/nod mode were executed.

### 2.2. High-pass Filter

MIR images generally show dusty structures, dust-embedded sources, stellar sources, and even emission from the mini-spiral. Overlapping wings of point-spread functions (PSFs) can create artificial sources and together with noise can complicate the identification of extended objects of interest, especially in a crowded FOV as in the central few arcseconds of the GC. In order to obtain high-angular-resolution information and to highlight the structures of the extended sources, we produce high-pass filter maps. High-pass filters can be used as a sharpener and to resolve the objects that are close to the detection limit while preserving the shape of the extended objects. This filtering technique and its significance are described in detail in Mužić et al. (2007); see also Peißker et al. (2020a, 2021).

First, the Gaussian-smoothed (3–9 pixel Gaussian, corresponding to 0''375–0''405) version of the input image is subtracted from itself. After removing the negatives, the resulted image is smoothed again using a Gaussian whose size is adjusted depending on the required angular resolution and sensitivity. In Figure 1, we show the effectiveness of this technique for isolating the signals and thereby reducing the chance of confusion between nearby objects.

## 3. Results

### 3.1. Differential Map

To get a general idea of the direction of the bulk motion, we produce a differential map using the smooth-subtracted images from the 2006 and 2018 epochs. As illustrated in Figure 2,

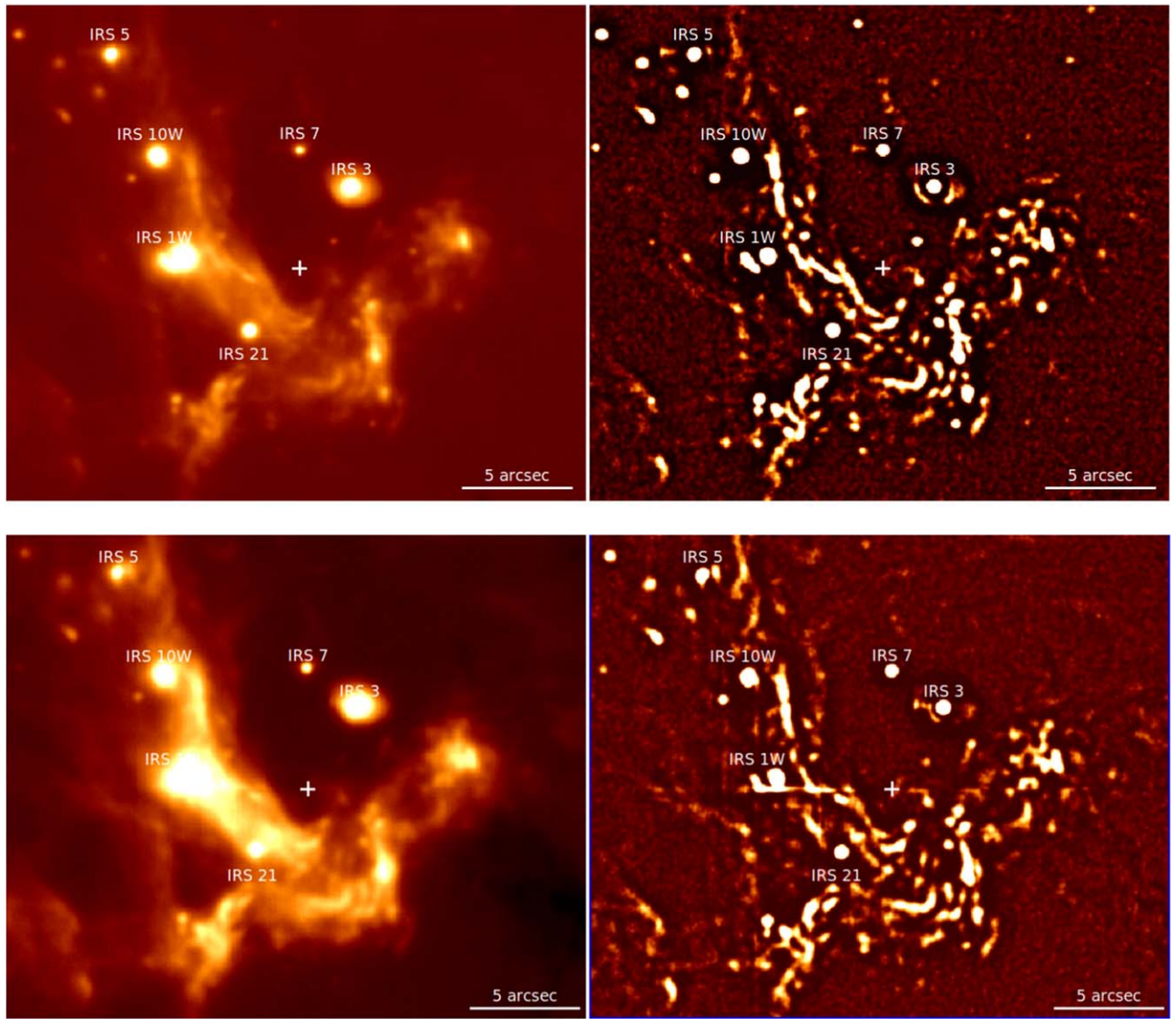


**Figure 1.** Central  $24'' \times 24''$  region of the Milky Way in the PAH1 filter ( $8.59 \mu\text{m}$ ) in the top panel and in the Ne II<sub>2</sub> filter ( $13.04 \mu\text{m}$ ) in the bottom panel. The north is up and the east is to the left. The right panel displays the high-pass-filtered version of the left image. All the dusty-filament-like structures and infrared-excess stars are resolved and enhanced through the high-pass filter.

subtracting the images separated by large timescales essentially represents the subtraction of two slightly shifted Gaussian profiles. The result is a crude but clear indication of the direction of the bulk motion. We first scaled (rebinned) and transformed all PAH1 image frames into the common coordinate system of the 2018 epoch using the positions of IRS 10EE, IRS 9, and IRS 7 (and Ne II<sub>2</sub> image frames using the positions of IRS 10EE, IRS 7, IRS 12N, IRS 15NE, and IRS 17) to calculate the transformation matrix. These positions were corrected for stellar velocities, as reported in the *K* band by Schödel et al. (2009) and Genzel et al. (2000). The resulting image (differential map) is presented in Figure 3 along with the derived proper motions of the stellar sources, which are discussed in subsequent subsections.

### 3.2. Proper Motions

We first identified the infrared sources (IRS) in *N*-band images by comparing them with the *K* and *L'* bands. To make sure the proper motions that we calculate are reliable, we make

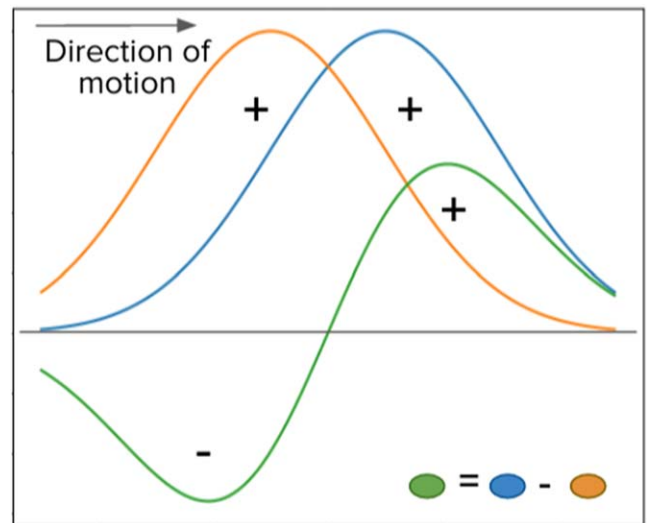


**Figure 2.** Difference of shifted Gaussian profiles as an indicator of the direction of motion.

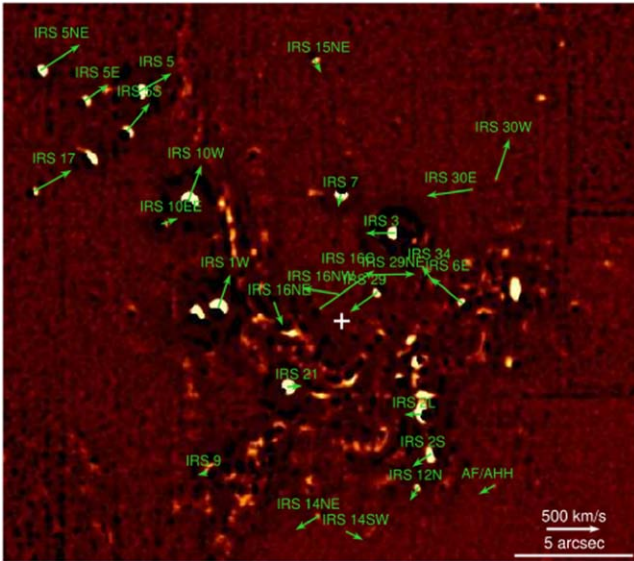


**Figure 3.** Differential map produced by subtracting the PAH1 2006 image from the PAH1 2018 image. The arrows correspond to velocities obtained by measuring offset positions and velocities w.r.t. IRS 10EE, 9, and 7.

similar calculations for IRS sources in the  $K$  band and compare them both with the velocities reported by Schödel et al. (2009) and Genzel et al. (2000). We chose IRS 10EE, IRS 9, IRS 12N, and IRS 7 as calibrators for PAH1 images (and IRS 10EE, IRS 7, IRS 12N, IRS 15NE, and IRS 17 for Ne II<sub>2</sub> images) as they were unambiguously identifiable in both  $N$  and  $K$  bands and had velocities,  $v_\alpha$  and  $v_\delta$ , from Schödel et al. (2009). We measure the offsets of each source of interest from these IRS sources. We calculate relative velocities w.r.t. each of them and then add their respective velocities (as given by Schödel et al. 2009), before averaging them to get the proper motions w.r.t. Sgr A\*. By doing so, we are minimizing the errors introduced during the process of offset measurements. As an example, we show in Figure 4 the  $v_\alpha$  and  $v_\delta$  plots for the source IRS 1W. Multiplying the proper motions with the distance to the GC,  $D_{GC} = 8.1$  kpc, gives the tangential velocity. We compare tangential velocities in the  $N$  band and  $K$  band with Schödel et al. (2009) and Genzel et al. (2000) in Appendix A. Table 5 in Appendix A contains the calculated velocities in various bands along with the literature values. Figures 12 and 13 in Appendix A depict the deviations from Schödel et al. (2009). It is important to note that the uncertainties in the fainter sources could be larger than in the brighter sources due to the possibility of unresolved background sources blending with our target sources. While the uncertainties of the Gaussian fits for the positions is typically of the order of a few hundredth of a pixel, we conservatively assume an uncertainty of 0.25 pixels for that quantity. The mean absolute difference between the velocities in the two filters is about  $100 \text{ km s}^{-1}$  and standard deviation of the angle difference is about  $40^\circ$ .

We then move on to calculate the tangential velocities of all the extended sources in the FOV, concentrating especially on the inner edge of the northern arm. We determine the positions of each resolved source by fitting an elliptical Gaussian using the data visualization tool QFitsView (Ott 2012). We derive tangential velocities as described above and tabulate them in Table 2. We only report velocities of those sources that are free from confusion in at least three epochs. The uncertainties in the

combined R.A./decl. velocities are about  $\pm 120 \text{ km s}^{-1}$  and the uncertainties in the flight direction are about  $\pm 30^\circ$ . Figure 5 shows the source labels and the apertures used in the left panel and their derived proper motion vectors in the right panel. We have removed the velocity vectors belonging to the IRS sources to get a clear indication of any bulk motion. We see a clear stream-like motion along the inner edge of the northern arm toward the southwest direction, which changes direction sharply as it crosses the Sgr A\* to move in the northwest direction (blue dashed arrow in Figure 6).

We assume that within the area of the mini-spiral's northern arm we find  $N_{NA}$  sources that truly belong to the northern arm. The number of sources in that region which belong to the underlying cluster is  $N_C$ . We assume that  $N_C$  is a fraction of  $N_{NA}$ , i.e.,

$$N_C = f \times N_{NA}. \quad (1)$$

The total number of sources detected within the area of the mini-spiral's northern arm is then given by

$$N_{\text{tot}} = N_C + N_{NA} = N_{NA} \times (1 + f). \quad (2)$$

Therefore, even if all the  $N_{NA}$  sources move downstream one would not expect that all sources observed in that region follow that trend. While we assume that all the  $N_{NA}$  sources in the northern arm will be headed downstream along the mini-spiral arm, we also assume in a very simplistic way that half of the cluster sources,  $N_C$ , in that area will be moving downstream and half of them upstream. This implies that the ratio,  $R$ , between the sources moving up- and downstream is

$$R = \frac{N_{NA} + 0.5 N_C}{0.5 N_C} = \frac{N_C/f + 0.5 N_C}{0.5 N_C} = \frac{2}{f} + 1. \quad (3)$$

As can be seen in Figure 5, we find that in the mini-spiral region 11 sources move downstream and four sources move upstream, implying  $R = 11/4 = 2.75$ . Hence, we find that

$$R = \frac{2}{f} + 1 = 2.75. \quad (4)$$

Therefore, that fraction,  $f$ , turns out to be just above unity, with

$$f = \frac{2}{2.75 - 1} = 1.14, \quad (5)$$

just as expected for an additional contribution of dusty infrared-excess sources due to the northern arm on top of a cluster contribution with conceivably almost the same number density in dusty, stellar infrared-excess sources. For an equal contribution from the northern arm and the cluster in the region of the northern arm, we would have expected  $R = 3$ .

### 3.3. Photometry

Even though there have been many photometric studies on stars in the GC in various other wavelengths, they are limited in the MIR (e.g., Blum et al. 1996; Ott et al. 1999; Tanner et al. 2002; Viehmann et al. 2005, 2006). We carry on these studies on the extended dusty sources that we have identified.

Viehmann et al. (2006) report flux densities in various filters including the  $N$  band. In the MIR regime, they performed relative aperture photometry while relying on Tanner et al. (2002) for flux calibration. Contrary to what is mentioned in Viehmann et al. (2006), it appears that the reported  $N$ -band flux densities are not extinction-corrected. For example,

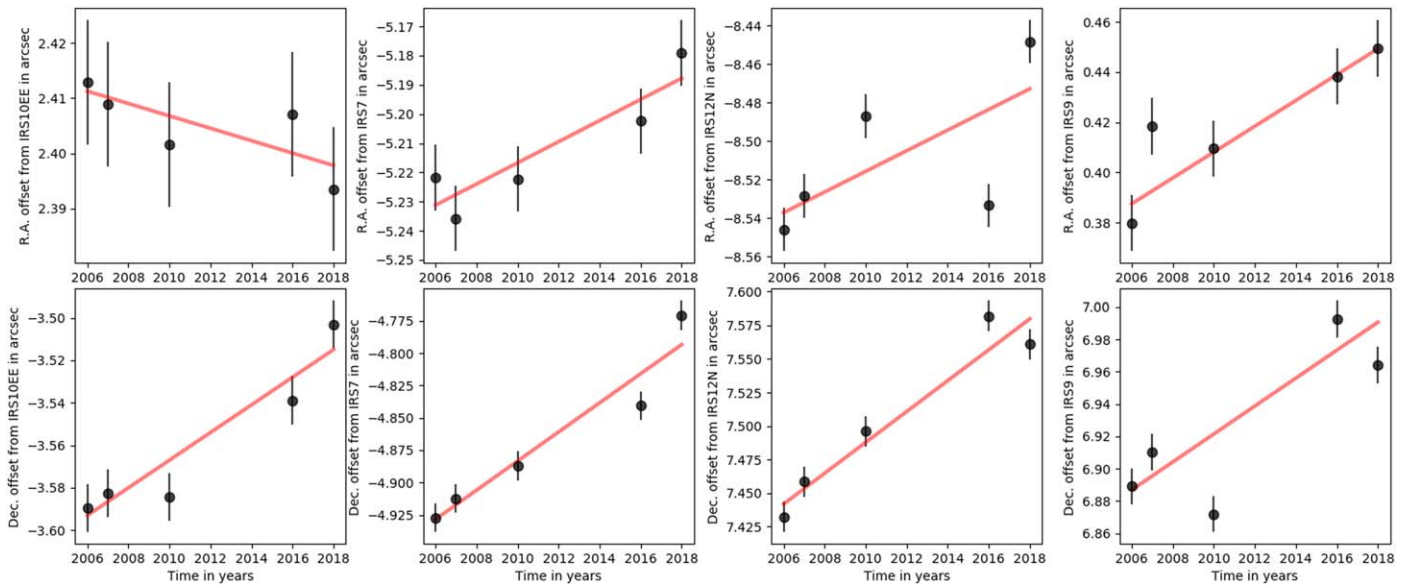


**Figure 4.** Proper motion,  $v_\alpha$  and  $v_\delta$ , of an example source IRS 1W. Relative velocities w.r.t. IRS 10EE, 7, 12N, and 9 were determined using offset measurements. Error bars correspond to 0.25 pixels.

Viehmman et al. (2006) report IRS 21’s flux density as 4.56 Jy at  $8.6 \mu\text{m}$ , which is consistent with 3.6 Jy by Stolovy et al. (1996) at  $8.7 \mu\text{m}$  and 3.6 by Tanner et al. (2002) at  $8.8 \mu\text{m}$ . Stolovy et al.’s (1996) results are based on the zero-point measurements made with SpectroCam-10 on the 200 inch Hale telescope. As both of these previous studies did not report dereddened fluxes, if Viehmman et al.’s (2006) values were, in fact, extinction-corrected we would expect it to be about 5 times higher. This finding is further confirmed by two other independent studies by N. B. Sabha et al. (2022, in preparation) and R. Schödel et al. (2022, in preparation; through private communication), both based on zero-point measurements provided by the ESO.

The flux densities were extracted via aperture photometry using elliptical apertures to match the shape of extended or filamentary sources (see Figure 5). Aperture sizes were determined by fitting a 2D Gaussian along the semimajor and semiminor axes of the source. We selected IRS 5NE, IRS 10W, IRS 7, and IRS 1W as calibrators using a source aperture and background similar to Viehmman et al. (2006). As all the elliptical apertures we use do not have the same area, we measured the surface density of background contribution at various apertures in the uncrowded regions of the image and multiplied it by the area of each ellipse to get their background contributions. An extinction correction of  $A_\lambda \sim 2.04$  for PAH1 and  $A_\lambda \sim 1.34$  for Ne II (Fritz et al. 2011) was applied to obtain dereddened flux densities.

Table 6 in Appendix B lists the flux density values by Viehmman et al. (2006), our results when we use similar apertures and background as Viehmman et al. (2006), and our results when we use aperture sizes determined by the FWHM of the 2D Gaussian that we fit (our results in the table are before extinction correction). The table shows that our calibration approach results in source flux densities that are in good agreement with the results from Viehmman et al. (2006). It is to be noted that the central wavelength of the Ne II\_2 filter used for our images is  $13.04 \mu\text{m}$  (Ne II\_2), while that of Viehmman et al.’s (2006) images is  $12.81 \mu\text{m}$  (Ne II). For  $\alpha_s \pm 1$  this difference corresponds to a 2% variation in flux densities.

Table 3 lists both the reddened ( $F$ ) and dereddened ( $F'$ ) flux densities of all the reliable sources at both PAH1 ( $8.59 \mu\text{m}$ ) and Ne II\_2 ( $13.04 \mu\text{m}$ ), along with their spectral indices, which were calculated using

$$\alpha_s = \frac{\log(F'_{13.04}/F'_{8.59})}{\log(8.59/13.04)}, \quad (6)$$

i.e., using the convention  $F \propto \nu^{+\alpha_s}$  or  $F \propto \lambda^{-\alpha_s}$ . In particular, hotter sources (nonembedded stars) are characterized by a positive spectral index in this convention, while dust-enshrouded stars, colder dusty filaments, or potential compact objects powered by nonthermal synchrotron emission (neutron stars) exhibit a steep power-law spectrum with a negative spectral index in the MIR domain.

In Figure 7, we depict the spectral indices of each source. The color and the size of each source indicate the spectral index and the flux density at the PAH1 band, respectively. In Figure 7, it is apparent that the brightest infrared-excess sources are also warm and blue, while the fainter and colder dust sources are along the mini-spiral.

### 3.4. Cometary Tail of IRS 7

IRS 7 (about  $5''.5$  north of Sgr A\*) is one of the brightest IR sources in the region and is classified as a pulsating M1/M2 red supergiant (Carr et al. 2000; Paumard et al. 2014; Gravity Collaboration et al. 2021). Radio (Yusef-Zadeh & Morris 1991; Yusef-Zadeh & Melia 1992) and MIR (Serabyn et al. 1991) observations of IRS 7 have revealed a bow-shock feature toward the north and a cometary-tail-like structure pointed directly away from Sgr A\*. Recently, Tsuboi et al. (2020) also reported the shell-like structure surrounding IRS 7 and its northern extension in the H30 $\alpha$  recombination line. They measured line-of-sight velocities and concluded that the tail is the gas stream flowing from the shell around IRS 7. As IRS 7 moves southward, the pulsating release of gas as a stellar wind (Paumard et al. 2014) is left behind and is ionized by far-UV radiation coming from the NSC.

**Table 2**  
List of Tangential Velocities

Source	Name	$\Delta\alpha$ (arcsec)	$\Delta\delta$ (arcsec)	$v_\alpha$	PAH1	Ne II_2	
					$v_\delta$	$v_\alpha$	$v_\delta$
(all velocities are in $\text{km s}^{-1}$ )							
1	IRS 5NE	12.71	10.55	-374	243	-167	-167
2	IRS 5E	10.87	9.27	-232	155	-216	-211
3	IRS 5S	9.07	7.97	-218	268	-75	97
4	IRS 5	8.53	9.67	-303	167	-71	-145
5		10.60	6.87	-223	286	-226	1
6	IRS 17	12.97	5.45	-351	198	-238	-83
7		6.75	12.08	-151	-345	-187	-279
8		6.68	9.95	-350	-472	-55	-52
9		5.00	8.10	-210	-96		
10	IRS 15NE	1.17	11.04	-67	-133	-6	-308
11	IRS 10EE	7.60	4.07	-157	54	-186	142
12	IRS 10W	6.45	5.08	-118	331	120	148
13	IRS 7	0.03	5.34	27	-125	232	-250
14	IRS 3	-2.26	3.70	282	-2	412	-13
15		4.90	4.41	-77	-3	-7	-182
16		4.69	2.97	-180	-132	-215	-215
17		6.10	0.24	159	178	20	-51
18	IRS 1W	5.21	0.57	-113	307	53	275
19		3.67	0.22	-221	-337	301	-218
20		2.34	-0.40	-360	-330	163	-205
21		3.54	-1.67	-136	-162	-25	-303
22	IRS 21	2.29	-2.78	-137	8	-65	3
23		1.47	-2.07	38	-93	196	17
24		-1.57	-0.53	-116	218	-170	39
25		-0.78	-1.61	-108	207	-180	255
26		-0.33	-2.44	-61	-225	-395	-33
27		10.00	-8.83	-21	-181	-62	-159
28		7.10	-7.83	-184	-80	173	-277
29		5.70	-7.86	-74	-120	-259	-455
30		5.60	-5.89	-16	-138	63	-175
31		4.82	-6.39	-89	-228	316	37
32		14.38	-5.71	-128	61	-72	-161
33		11.07	-5.41	-191	-160	-44	-267
34		10.47	-5.97	103	-313	-135	-7
35		6.61	-1.80	-142	-126	-141	-195
36		6.35	-2.96	20	-157	64	-193
37		2.84	-5.14	-126	63	-185	7
38		3.66	-5.29	-53	-70	55	-3
39		0.26	-3.57	-51	-209	-189	-198
40		-1.14	-4.07	-98	-52	-57	-353
41		-1.41	-3.06	-139	166	6	-209
42		-2.47	-2.42	86	180	76	175
43		0.58	-1.94	-50	5	-295	-7
44	IRS 29	-1.50	1.22	256	-186	585	-205
45		-3.54	2.05	-71	374	-89	502
46		-3.19	-1.67	41	144	93	122
47	IRS 2L	-3.39	-3.94	173	-2	293	191
48		-5.44	2.50	198	92	362	74
49		-5.39	1.39	36	138	699	92
50		-5.90	0.33	-74	104	418	92
51		-6.00	-1.03	202	-87	100	185
52		-4.34	-1.70	-61	-21	185	180
53		-5.24	-0.11	-27	45	546	-85
54		-7.12	-1.73	329	206	368	-79
55		-7.75	-0.19	203	-81	273	158
56		-8.30	1.38	-297	20	98	181
57		-9.82	0.67	-32	438	123	179
58		-7.36	1.28	96	234	15	160
59		2.66	-4.41	-46	93	-84	357
60	IRS 2S	-3.78	-5.59	180	-124	82	-230
61		-2.81	-5.53	27	-168	-255	-15
62		-2.23	-5.60	-230	-137	168	-139

**Table 2**  
(Continued)

63		-3.10	-4.81	-79	-13	331	36
64		-2.45	-4.47	30	166	-71	287
65		-1.63	-5.04	-49	-149	-366	145
66		-4.24	-7.01	-222	132	-100	-24
67	IRS 12N	-3.24	-6.99	80	-133	-5	-106
68		-3.01	-6.11	-39	-50	-127	123
69		-1.97	-6.56	91	-310	-326	-66
70		-4.52	-5.99	-191	-52	1	343
71		4.42	1.53	351	259	132	-271
72		3.55	1.47	-72	-68	-150	-244
73		3.85	3.01	-373	-419	334	-96
74		3.26	3.35	48	220	-21	-593
75		3.77	7.10	-16	188		
76		3.60	6.23	-22	261	-146	-338
77		3.24	5.16	47	105	108	173
78		0.02	8.46	302	231		
79		-0.09	7.73	297	211	516	126
80		-0.27	7.16	268	-301	990	250
81		-2.30	8.38	-193	340	970	-529
82		10.44	1.18	-90	189		
83		8.87	0.49	-27	207		
84		4.25	1.91	41	-273		
85	IRS 16NE	2.87	0.81	-83	-224		
86		1.27	0.85	-289	-79		
87	IRS 16C	0.93	0.51	-513	358		
88	IRS 16NW	0.12	1.13	351	54		
89	IRS 29NE	-1.15	1.93	-435	7		
90	IRS 9	5.66	-6.40	97	-22		
91		1.59	-0.53	-227	-289		
92		1.13	-1.39	88	102		
93		-1.89	-2.02	-95	42		
94		-2.53	-1.41	150	220		
95		-2.92	-0.88	114	247		
96	IRS 34	-3.91	1.56	119	166		
97		-6.37	2.97	-36	112		
98		-6.98	2.90	237	-133		
99		-6.72	2.42	-60	118		
100		1.69	-4.39	-88	-190	-100	-91
101		0.87	-3.12	-335	-538		
102		-0.39	-3.15	-258	81	-105	-43
103		-0.69	-3.69	-342	-47		
104		-1.90	-3.22	24	166	-205	13
105		1.35	-6.69	80	-113	112	100
106		1.30	-7.13	-65	-157		
107	IRS 14NE	0.95	-8.22	223	-130	153	-91
108		-1.25	-8.69	-47	-546		
109		3.66	-11.41	-3	-456		
110		4.24	-8.74	5	-164		
111		4.28	-7.38	-20	-195		
112		3.75	-7.31	82	-316		
113		3.00	-7.70	-213	-235		
114		2.68	-7.26	-367	-5		
115		3.07	-6.62	-24	-84	-458	338
116		3.08	-5.82	77	18		
117	IRS 30E	-5.52	5.53	435	-59		
118	IRS 30W	-6.50	5.94	-125	384		
119	IRS 6E	-5.07	0.76	294	234	398	181
120	AF/AHH	-6.46	-6.93	152	-85		
121	IRS 14SW	-0.18	-8.88	-162	-80		

**Note.** The positions are offsets from Sgr A\* (in 2018) in arcsecs and all the velocities are in  $\text{km s}^{-1}$ . We chose a conservative 0.25 pixel uncertainty for proper motion calculations, which corresponds to about  $45 \text{ km s}^{-1}$ .

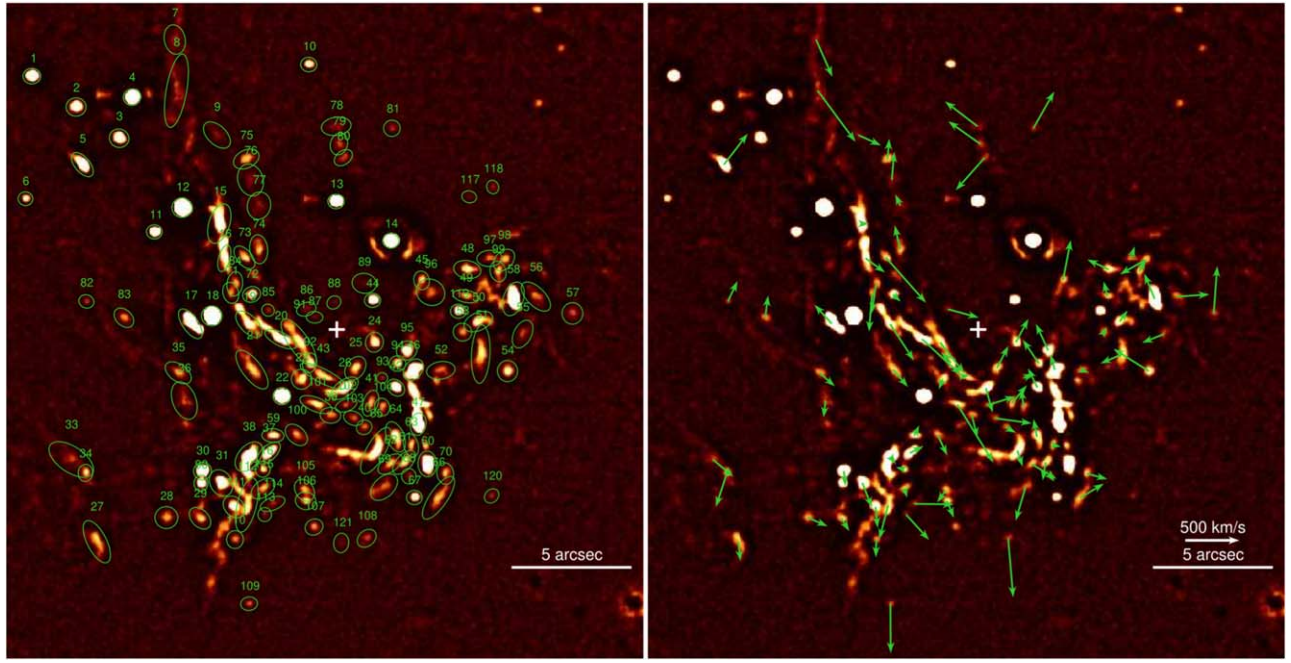


**Figure 5.** Left: the PAH1 image with the identification for each source and the apertures used to perform photometry. Right: proper motion of all the labeled sources. Arrows corresponding to IRS sources are removed for a better visualization of the stream-like motion.

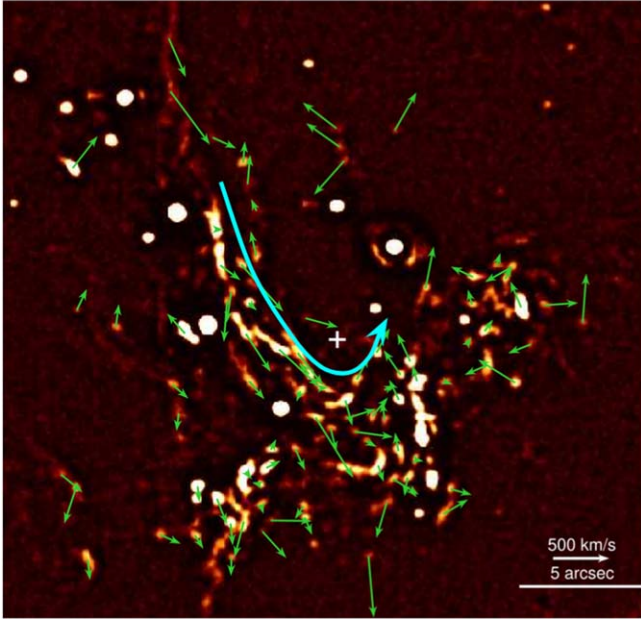


**Figure 6.** Presence of a stream-like motion along the inner edge of the northern arm toward the southwest direction, which changes direction sharply as it crosses the Sgr A\* to move in the northwest direction (blue dashed arrow).

In the right panel of Figure 8, we show the PAH1 ( $8.59 \mu\text{m}$ ) image of IRS 7 and its extended tail in comparison with the  $\lambda = 2 \text{ cm}$  contour map from Yusef-Zadeh & Melia (1992), which is on the left. Contours of individual substructures of the tail in both wavelengths seem to match well with each other, which is an indication of the quality of our data and filtering techniques. The tail extends from  $1''$  to  $3''.6$  north of IRS 7 and has three major substructures. Blue arrows mark the proper motions and gray lines mark their error boundaries. The slight discrepancy in the direction of the transverse velocity in the MIR/near-IR bands (see Appendix A), and by using SiO maser astrometry

(Reid et al. 2003; Borkar et al. 2020), could be caused by the fact that they probe different layers of the star. The proper-motion measurements of the substructures of the tail reveal the dominant influences on each of them. The northern two, which have detached from IRS 7 earliest, have almost similar velocities. This could mean that they are driven by a nuclear outflow coming from the inner few arcseconds.

In addition, the proper-motion distribution of the three components reflects the combination of the downstream fluid motion in the IRS 7 tail and the development of hydrodynamic instabilities, such as Kelvin–Helmholtz (KH) instabilities, which are manifested as propagating waves moving transverse along the south–north direction of the flow, i.e., they introduce an additional turbulent velocity field to the predominant south–north downstream bow-shock flow. The development of the KH instability is expected due to the velocity shear between the shocked stellar wind of IRS 7 and the surrounding hot medium. Assuming that the MIR–radio tail clumps formed due to the KH instability, we adopt their typical length scale,  $\lambda_{\text{tail}} \sim 0''.5 \sim 0.02 \text{ pc}$ , from Figure 8. The density and the temperature of the tail components,  $n_{\text{tail}} \sim 6 \times 10^4 \text{ cm}^{-3}$  and  $T_{\text{tail}} \sim 4650 \text{ K}$ , respectively, can be inferred from H30 $\alpha$  recombination-line observations (Tsuboi et al. 2020). These tail components are approximately in pressure equilibrium with the surrounding hot medium, under the assumption of the extrapolation of the Bondi-radius values,  $T_a \sim 10^7 \text{ K}$  and  $n_a \sim 26 \text{ cm}^{-3}$  (Baganoff et al. 2003), i.e.,  $n_{\text{tail}} T_{\text{tail}} \sim n_a T_a$ . This implies a density ratio between the ambient medium and the IRS 7 tail of  $r = n_a/n_{\text{tail}} \sim 4.3 \times 10^{-4}$ . For the shear velocity, we take the mean of the IRS 7 stellar motions,  $v_{\text{shear}} \simeq v_* \sim 180 \text{ km s}^{-1}$ , according to Table 5. The growth timescale of KH instabilities of the size  $\lambda_{\text{tail}}$  can be estimated as

$$\tau_{\text{KH}} \sim \frac{\lambda_{\text{tail}}}{v_{\text{shear}}} \frac{1+r}{\sqrt{r}} \sim 111 \text{ yr}. \quad (7)$$

Since the crossing timescale of the IRS 7 for the total length of the tail,  $l_{\text{tail}} \sim 3''$ , is  $\tau_{\text{cross}} \sim l_{\text{tail}}/v_* \sim 652 \text{ yr} \gtrsim \tau_{\text{KH}}$ , the KH



**Table 3**  
List of Reliable Flux Densities in PAH1 and Ne II<sub>2</sub> Filters

Source	Name	$F_{8.59}$ (Jy)	$\Delta F_{8.59}$ (Jy)	$F'_{8.59}$ (Jy)	$\Delta F'_{8.59}$ (Jy)	$F_{13.04}$ (Jy)	$\Delta F_{13.04}$ (Jy)	$F'_{13.04}$ (Jy)	$\Delta F'_{13.04}$ (Jy)	$\alpha_s$	$\Delta\alpha_s$
1	IRS 5NE	0.57	0.09	3.75	0.58	1	0.09	3.43	0.3	0.21	0.43
2	IRS 5E	0.49	0.08	3.22	0.50	1.99	0.17	6.84	0.58	-1.80	0.42
3	IRS 5S	0.61	0.09	4.01	0.62	2.35	0.2	8.07	0.69	-1.68	0.42
4	IRS 5	3.92	0.60	25.64	3.90	4.54	0.38	15.58	1.32	1.19	0.42
5		0.54	0.08	3.50	0.54	1.83	0.16	6.3	0.54	-1.41	0.42
6	IRS 17	0.02	0.01	0.11	0.02	0.27	0.02	0.94	0.09	-5.14	0.49
7		0.33	0.05	2.18	0.34	3.47	0.29	11.91	1.01	-4.07	0.43
8		1.38	0.21	9.02	1.39	6.33	0.54	21.73	1.84	-2.11	0.42
9		0.21	0.03	1.38	0.22	5.36	0.46	18.43	1.56	-6.21	0.43
10	IRS 15NE	0.04	0.01	0.26	0.05	0.09	0.01	0.3	0.03	-0.34	0.52
11	IRS 10EE	0.46	0.07	3.02	0.47	1.22	0.1	4.19	0.36	-0.78	0.43
12	IRS 10W	8.33	1.27	54.51	8.28	11.61	0.98	39.87	3.36	0.75	0.42
13	IRS 7	1.15	0.18	7.54	1.15	2.04	0.17	7	0.6	0.18	0.42
14	IRS 3	8.65	1.31	56.59	8.60	11.75	0.99	40.37	3.4	0.81	0.42
15		4.00	0.61	26.17	3.99	9.39	0.79	32.26	2.72	-0.50	0.42
16		1.64	0.25	10.73	1.64	9.27	0.78	31.83	2.69	-2.60	0.42
17		6.67	1.01	43.64	6.63	11.87	1	40.76	3.44	0.16	0.42
18	IRS 1W	16.14	2.45	105.66	16.05	21.97	1.85	75.47	6.36	0.81	0.42
19		3.99	0.61	26.15	3.98	12.64	1.07	43.44	3.67	-1.22	0.42
20		3.03	0.46	19.85	3.02	5.28	0.45	18.14	1.53	0.22	0.42
21		3.54	0.54	23.19	3.53	12.48	1.05	42.86	3.62	-1.47	0.42
22	IRS 21	4.79	0.73	31.39	4.77	6.92	0.58	23.77	2.01	0.67	0.42
23		2.37	0.36	15.52	2.36	11.58	0.98	39.79	3.36	-2.26	0.42
24		0.49	0.08	3.24	0.50	1.49	0.13	5.11	0.44	-1.09	0.42
25		0.81	0.12	5.28	0.81	2.34	0.2	8.02	0.68	-1.00	0.42
26		1.86	0.28	12.18	1.86	6.16	0.52	21.15	1.79	-1.32	0.42
27		0.42	0.07	2.74	0.43	2.78	0.24	9.54	0.81	-2.99	0.43
28		0.33	0.05	2.13	0.33	1.78	0.15	6.12	0.52	-2.53	0.42
29		0.74	0.11	4.82	0.74	3.61	0.31	12.39	1.05	-2.26	0.42
30		1.10	0.17	7.18	1.10	2.95	0.25	10.14	0.86	-0.83	0.42
31		2.26	0.35	14.81	2.26	6.09	0.52	20.92	1.77	-0.83	0.42
32		0.60	0.09	3.91	0.61	4.45	0.38	15.28	1.3	-3.27	0.43
33		0.49	0.08	3.19	0.50	3.44	0.29	11.83	1.01	-3.14	0.43
34		0.18	0.03	1.15	0.18	1.89	0.16	6.48	0.55	-4.14	0.43
35		0.59	0.09	3.87	0.60	2.99	0.25	10.28	0.87	-2.34	0.42
36		0.59	0.09	3.86	0.60	2.65	0.23	9.11	0.78	-2.06	0.43
37		1.32	0.20	8.65	1.32	3.72	0.32	12.79	1.08	-0.94	0.42
38		3.05	0.47	19.98	3.04	8.05	0.68	27.67	2.34	-0.78	0.42
39		0.96	0.15	6.29	0.96	4.24	0.36	14.56	1.23	-2.01	0.42
40		0.58	0.09	3.78	0.58	2.25	0.19	7.72	0.66	-1.71	0.42
41		0.81	0.12	5.30	0.81	2.05	0.17	7.04	0.6	-0.68	0.42
42		1.06	0.16	6.92	1.06	2.26	0.19	7.77	0.66	-0.28	0.42
43		2.33	0.36	15.24	2.33	6.6	0.56	22.68	1.92	-0.95	0.42
44	IRS 29	0.13	0.02	0.85	0.14	0.14	0.01	0.48	0.05	1.37	0.47
45		0.14	0.02	0.94	0.15	0.61	0.05	2.09	0.18	-1.91	0.43
46		2.41	0.37	15.80	2.41	4.08	0.35	14	1.19	0.29	0.42
47	IRS 2L	3.28	0.50	21.49	3.27	5.52	0.47	18.98	1.6	0.30	0.42
48		0.64	0.10	4.20	0.65	1.48	0.13	5.09	0.44	-0.46	0.42
49		0.57	0.09	3.72	0.57	2.5	0.21	8.6	0.73	-2.01	0.42
50		1.33	0.20	8.71	1.33	4.11	0.35	14.14	1.2	-1.16	0.42
51		1.60	0.25	10.49	1.61	5.88	0.5	20.21	1.71	-1.57	0.42
52		0.97	0.15	6.34	0.97	7.58	0.64	26.04	2.21	-3.38	0.42
53		0.46	0.07	3.01	0.46	1.51	0.13	5.17	0.44	-1.30	0.42
54		0.34	0.05	2.24	0.35	1.39	0.12	4.79	0.41	-1.82	0.43
55		0.55	0.09	3.61	0.56	2.09	0.18	7.19	0.61	-1.65	0.42
56		0.82	0.13	5.38	0.83	3.65	0.31	12.55	1.07	-2.03	0.42
57		0.03	0.01	0.22	0.04	0.47	0.04	1.61	0.14	-4.77	0.48
58		4.07	0.62	26.65	4.06	7.26	0.61	24.95	2.11	0.16	0.42
59		0.66	0.10	4.34	0.67	2.77	0.23	9.5	0.81	-1.88	0.42
60	IRS 2S	1.93	0.29	12.64	1.93	3.67	0.31	12.61	1.07	0.01	0.42
61		1.68	0.26	11.00	1.68	4.4	0.37	15.1	1.28	-0.76	0.42
62		1.37	0.21	8.97	1.37	5.63	0.48	19.36	1.64	-1.84	0.42
63		1.73	0.26	11.36	1.73	3.83	0.32	13.17	1.12	-0.35	0.42

**Table 3**  
(Continued)

Source	Name	$F_{8.59}$ (Jy)	$\Delta F_{8.59}$ (Jy)	$F'_{8.59}$ (Jy)	$\Delta F'_{8.59}$ (Jy)	$F_{13.04}$ (Jy)	$\Delta F_{13.04}$ (Jy)	$F'_{13.04}$ (Jy)	$\Delta F'_{13.04}$ (Jy)	$\alpha_s$	$\Delta\alpha_s$
64		2.34	0.36	15.34	2.34	7.67	0.65	26.37	2.23	-1.30	0.42
65		3.86	0.59	25.27	3.85	9.92	0.84	34.1	2.88	-0.72	0.42
66		0.73	0.11	4.75	0.73	1.03	0.09	3.54	0.31	0.70	0.42
67	IRS 12N	0.16	0.03	1.05	0.17	0.42	0.04	1.46	0.13	-0.79	0.44
68		0.42	0.07	2.77	0.43	1.03	0.09	3.55	0.3	-0.59	0.42
69		0.80	0.12	5.21	0.80	5.9	0.5	20.28	1.72	-3.26	0.42
70		0.36	0.06	2.36	0.37	1	0.09	3.44	0.3	-0.90	0.43
71		2.02	0.31	13.20	2.01	5.43	0.46	18.64	1.58	-0.83	0.42
72		1.04	0.16	6.82	1.04	1.94	0.17	6.68	0.57	0.05	0.42
73		1.08	0.17	7.09	1.08	1.98	0.17	6.82	0.58	0.09	0.42
74		0.64	0.10	4.18	0.65	2.09	0.18	7.18	0.61	-1.30	0.42
75		0.39	0.06	2.56	0.40	1.12	0.1	3.85	0.33	-0.98	0.43
76		0.50	0.08	3.27	0.51	1.22	0.11	4.2	0.36	-0.60	0.43
77		0.30	0.05	1.98	0.31	0.78	0.07	2.69	0.23	-0.73	0.43
78		0.01	0.01	0.05	0.02	0.08	0.01	0.27	0.03	-4.04	0.99
79		0.02	0.01	0.14	0.03	0.1	0.01	0.35	0.04	-2.20	0.58
80		0.02	0.01	0.16	0.03	0.09	0.01	0.3	0.03	-1.51	0.51
81						0.01	0.01	0.03	0.01		
82		0.01	0.01	0.09	0.02						
83		0.30	0.05	1.96	0.31						
84		1.69	0.26	11.05	1.69						
85	IRS 16NE	0.50	0.08	3.26	0.50						
86		0.02	0.01	0.12	0.02						
87	IRS 16C	0.01	0.01	0.05	0.01						
88	IRS 16NW										
89	IRS 29NE	0.01	0.01	0.04	0.02						
90	IRS 9	0.78	0.12	5.14	0.79						
91		3.73	0.57	24.39	3.72	9.83	0.83	33.77	2.86	-0.78	0.42
92		1.15	0.18	7.54	1.15						
93		0.19	0.03	1.22	0.19	1.24	0.11	4.27	0.37	-3.00	0.43
94		0.85	0.13	5.55	0.85	3.28	0.28	11.26	0.96	-1.69	0.42
95		1.15	0.18	7.50	1.15	4.24	0.36	14.58	1.24	-1.59	0.42
96	IRS 34	0.44	0.07	2.86	0.45						
97		0.50	0.08	3.25	0.50	0.97	0.08	3.33	0.29	-0.06	0.42
98		0.57	0.09	3.74	0.58	2.29	0.2	7.87	0.67	-1.78	0.42
99		0.85	0.13	5.57	0.85	2.43	0.21	8.34	0.71	-0.97	0.42
100		0.88	0.13	5.76	0.88	6.17	0.52	21.19	1.79	-3.12	0.42
101		1.94	0.30	12.67	1.93	6.48	0.55	22.26	1.88	-1.35	0.42
102		0.72	0.11	4.72	0.72	3.14	0.27	10.8	0.92	-1.98	0.42
103		0.56	0.09	3.68	0.57	2.03	0.17	6.98	0.59	-1.53	0.42
104		0.52	0.08	3.42	0.53	1.61	0.14	5.52	0.47	-1.15	0.42
105		0.46	0.07	3.01	0.47	3.54	0.3	12.15	1.03	-3.34	0.43
106		0.29	0.05	1.92	0.30	1.5	0.13	5.14	0.44	-2.36	0.43
107	IRS 14NE	0.01	0.01	0.07	0.02						
108						0.14	0.01	0.47	0.05		
109											
110		0.43	0.07	2.80	0.43	1.84	0.16	6.31	0.54	-1.95	0.42
111		2.18	0.33	14.24	2.17	5.94	0.5	20.41	1.73	-0.86	0.42
112		3.85	0.59	25.22	3.84						
113		0.15	0.02	1.00	0.16	0.76	0.07	2.6	0.22	-2.29	0.43
114		0.24	0.04	1.54	0.24	0.96	0.08	3.28	0.28	-1.81	0.43
115		0.88	0.14	5.78	0.89	2.45	0.21	8.41	0.72	-0.90	0.42
116		0.76	0.12	4.96	0.76	1.13	0.1	3.87	0.33	0.59	0.42
117	IRS 30E										
118	IRS 30W										
119	IRS 6E	0.39	0.06	2.53	0.39	1.22	0.1	4.19	0.36	-1.21	0.42
120	AF/AHH										
121	IRS 14SW										

instabilities of the length scale of the observed clumps could have developed as IRS 7 plows through the hot medium. The KH instabilities of the radius  $R_{\text{tail}} \sim 0.5\lambda_{\text{tail}}$  can also survive

long enough in the surrounding hot medium to be observed. For the pressure-confined colder clumps of the constant mass density  $\rho_{\text{tail}}$  that have a mass of  $m_{\text{tail}} = 4/3\pi R_{\text{tail}}^3 \rho_{\text{tail}}$ , the

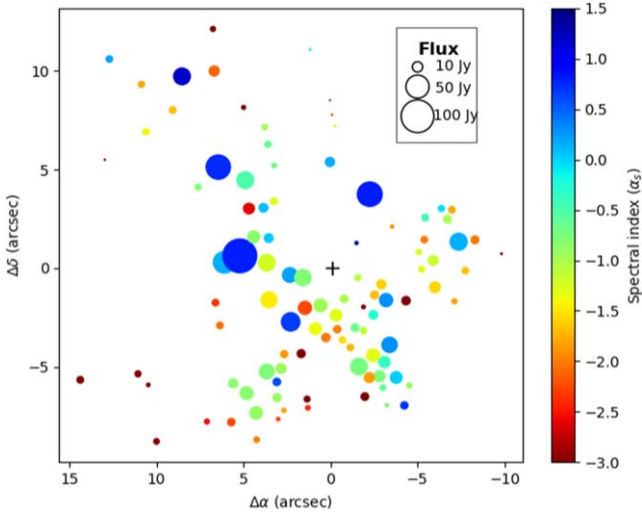


**Figure 7.** Spectral indices using the dereddened flux density measurements in the PAH1 and Ne II<sub>2</sub> filters. The positions are offsets from Sgr A\* and the sizes correspond to the flux density in the PAH1 filter. The figure also shows the positive correlation between the PAH1 flux density and the spectral index ( $\alpha_s$ ): the larger the PAH1 flux density (larger circles), the greater the spectral index (bluer colors).

evaporation timescale is given by Cowie & McKee (1977) and Karas et al. (2021):

$$\begin{aligned} \tau_{\text{evap}} &= \frac{25k_B n_{\text{tail}} R_{\text{tail}}^2}{8\kappa_{\text{H}}} \\ &\simeq 4067 \left( \frac{n_{\text{tail}}}{6 \times 10^4 \text{ cm}^{-3}} \right) \left( \frac{R_{\text{tail}}}{0.02 \text{ pc}} \right)^2 \text{ yr}, \end{aligned} \quad (8)$$

where  $\kappa_{\text{H}}$  is the conductivity of the hot ambient medium, and its value can be calculated as  $\kappa_{\text{H}} = 1.92 \times 10^{11} \text{ erg s}^{-1} \text{ K}^{-1} \text{ cm}^{-1}$ . Since  $\tau_{\text{KH}} < \tau_{\text{cross}} < \tau_{\text{evap}}$ , the KH instabilities can properly explain the tail components of IRS 7.

### 3.5. Extended Emission of IRS 3

IRS 3 is the brightest and the most extended stellar source at the GC. Although it is a stellar core, the extended source is not circularly symmetric, which has been a topic of interest. Viehmann et al. (2005) suggests that this morphology is due to a bow shock generated by winds from the massive central stellar cluster or an outflow from Sgr A\*. However, Yusef-Zadeh et al. (2017) suggests a tidal distortion scenario as IRS 3 orbits around Sgr A\*. In Figure 9, we compare the contour maps around IRS 3 with a 226 GHz image from Yusef-Zadeh et al. (2017).

By comparing the 226 GHz emission and the PAH1 image in Figure 9, the IRS3 circumstellar envelope exhibits similar structures at both wavelengths, in particular the extension in the northeast/southwest direction as well as another brighter extension to the southeast. Since the circumstellar material of IRS 3 has an enormous radius of  $R_{\text{IRS3}} \sim 1'' \sim 0.04 \text{ pc} \sim 2 \times 10^6 R_{\odot}$ , i.e., a thousand times bigger than a red supergiant or an asymptotic giant branch (AGB) star, it could be a signature of tidal elongation along the proper-motion direction as suggested by Yusef-Zadeh et al. (2017). The question arises: What could have caused the expansion of the IRS 3 envelope beyond its tidal (Hill) radius? If we consider the upper limit on the distance of IRS 3 from Sgr A\* based on its mean stellar velocity of

$v_* \sim 266 \text{ km s}^{-1}$  (see Table 5), we obtain

$$d_{\text{IRS3}} \lesssim 0.24 \text{ pc}. \quad (9)$$

Then we can estimate the upper limit on the tidal radius of IRS 3:

$$\begin{aligned} R_{\text{tidal}} &\lesssim d_{\text{IRS3}} \left( \frac{m_{\text{IRS3}}}{3M_*} \right)^{1/3} \\ &\sim 10^5 \left( \frac{d_{\text{IRS3}}}{0.24 \text{ pc}} \right) \left( \frac{m_{\text{IRS3}}}{10 M_{\odot}} \right)^{1/3} \left( \frac{M_*}{4 \times 10^6 M_{\odot}} \right)^{-1/3} R_{\odot}. \end{aligned} \quad (10)$$

Hence, even the largest red supergiants or AGB stars should have photospheres well inside their tidal radii at the distance of IRS 3; see Equation (9). One possibility of the perturbation of the atmosphere of IRS 3 is its ongoing or recent past interaction with the fast nuclear outflow or the jet, which led to shock propagation inside the red supergiant's envelope. This could effectively lead to atmosphere ablation by the jet (Zajaček et al. 2020a). As a consequence, after one jet crossing, the IRS 3 envelope adiabatically puffed up beyond the tidal (Hill) radius of the host star. The shocked envelope would expand adiabatically up to the tidal radius on the timescale given by the sound speed,

$$\begin{aligned} \tau_{\text{exp}} &\sim \frac{R_{\text{tidal}}}{c_s} \\ &\simeq 172 \left( \frac{R_{\text{tidal}}}{10^5 R_{\odot}} \right) \left( \frac{T_{\text{atm}}}{10^4 \text{ K}} \right)^{-1/2} \text{ yr}, \end{aligned} \quad (11)$$

where  $T_{\text{atm}}$  is the temperature of the shocked red-giant envelope or the temperature of the red-giant photosphere after the jet ablation.

Subsequently, after the short envelope expansion up to the tidal radius, the red-giant circumstellar material further undergoes tidal prolongation along the orbital direction. The tidal stretching generally takes place on a timescale that is a fraction of the orbital timescale. The prolongation of an envelope of a radius  $R_{\text{tidal}}$  by a factor of  $m = 10$  is expected to occur in

$$\begin{aligned} \tau_{\text{tidal}} &= \sqrt{m} \frac{d_{\text{IRS3}}^{3/2}}{\sqrt{GM_*}}, \\ &= 2772 \left( \frac{m}{10} \right)^{1/2} \left( \frac{d_{\text{IRS3}}}{0.24 \text{ pc}} \right)^{3/2} \left( \frac{M_*}{4 \times 10^6 M_{\odot}} \right)^{-1/2} \text{ yr}. \end{aligned} \quad (12)$$

Hence, the current extended state of IRS 3 is likely the result of its atmosphere's perturbation by the fast outflow or the jet, which led to a propagating shock inside the red-giant envelope. This was followed by fast envelope expansion up to the tidal radius, and subsequently tidal prolongation along IRS 3's orbital motion took place. Both processes are characterized by timescales shorter than the orbital timescale,  $P_{\text{IRS3}} \sim 5508 (d_{\text{IRS3}}/0.24 \text{ pc})^{3/2} \text{ yr}$ . Hence, the current extended state of IRS 3 is the result of a recent interaction a few thousand years ago.

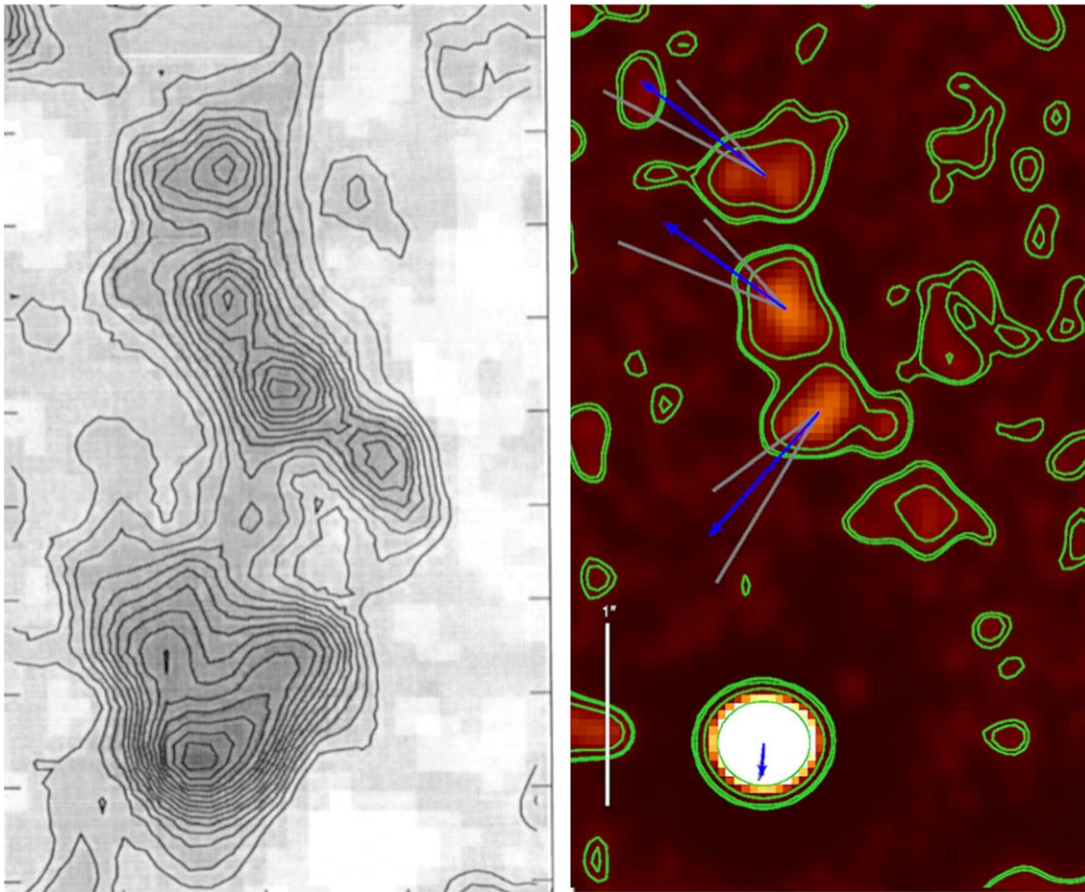


**Figure 8.** On the left is an image of IRS 7 and its extended tail at 2 cm from Yusef-Zadeh & Melia (1992), and on the right is a smooth-subtracted image with the same FOV in the PAH1 filter. The tail has three prominent substructures and their proper motions are indicated by blue arrows with gray lines as their error boundaries.

### 3.6. Nature of Dusty Sources

To get a better understanding of the nature of the dusty sources in the GC, it becomes important to perform statistical analysis of all their physical properties. We fit a 2D Gaussian on each source to determine its length and width (major and minor axes of the elliptical aperture). In the top-left image of Figure 10, we show a histogram of these measurements.

The distribution of position angles, measured anticlockwise from the west, is plotted in the top-right image of Figure 10. The sources along the northern arm have a smaller dispersion, which is expected given the fact they form a streamer-like structure.

The ellipticity, defined as  $(a - b)/a$ , where  $a$  and  $b$  are the major and minor axes (length and width here), is plotted in the bottom-left image of Figure 10. Lastly, the bottom-right image is a distribution of spectral indices. A large number of sources with negative indices reiterates the fact that the MIR region is dominated by dust-covered stars and colder dusty filaments.

In Figure 11, we try to find correlations between several fundamental physical properties of the dusty sources. In Table 4, we list the Spearman correlation coefficient,  $s$ , as well as the corresponding  $p$ -value for all possible combinations of parameters, in 21 pairs total. We find five significant positive correlations with sufficiently low  $p$ -values ( $p < 10^{-3}$ ): length–ellipticity, flux (Ne II<sub>2</sub>)–length, flux (Ne II<sub>2</sub>)–ellipticity, flux (PAH1)–flux (Ne II<sub>2</sub>), and flux (PAH1)–spectral index. The positive correlation between the length and the ellipticity is expected due to the definition of ellipticity, while no significant

correlation between the width and the ellipticity is caused by the narrow width distribution, which is caused by the lower cutoff due to the angular resolution, while the higher cutoff is likely determined rather by the physical process of the clump formation and evolution. The positive correlation between the flux densities at both wavelengths is also expected based on the spectral energy distribution for most of the dusty sources: with increasing wavelength, the flux density increases in the MIR domain. The positive correlation between the flux (PAH1) and the spectral index indicates that the differences among spectral energy distributions are mainly due to the flux density at  $8.59 \mu\text{m}$  (PAH1) rather than due to the flux density at  $13.04 \mu\text{m}$  (Ne II<sub>2</sub>). The flatter spectrum is caused by the higher PAH1 flux density, while the Ne II<sub>2</sub> filter flux density is not significantly correlated with the spectral index. This is also visible in Figure 7, where the most luminous sources in the PAH1 filter have a clear tendency toward the positive spectral index (the bigger the symbol, the bluer the color). This is also in line with the last two significant positive correlations: flux density (Ne II<sub>2</sub>) and the length of the filaments, i.e., the longer the filament, the larger the flux density in the Ne II<sub>2</sub> filter. On the other hand, the correlation between the PAH1 flux density and the length is weaker and less significant. The positive correlation between the Ne II<sub>2</sub> flux density and the filament ellipticity then stems from the definition of the ellipticity that includes the length.

The origin of the elongated blobs and filaments in the mini-spiral is uncertain. They could have arisen due to several processes, which we list below:

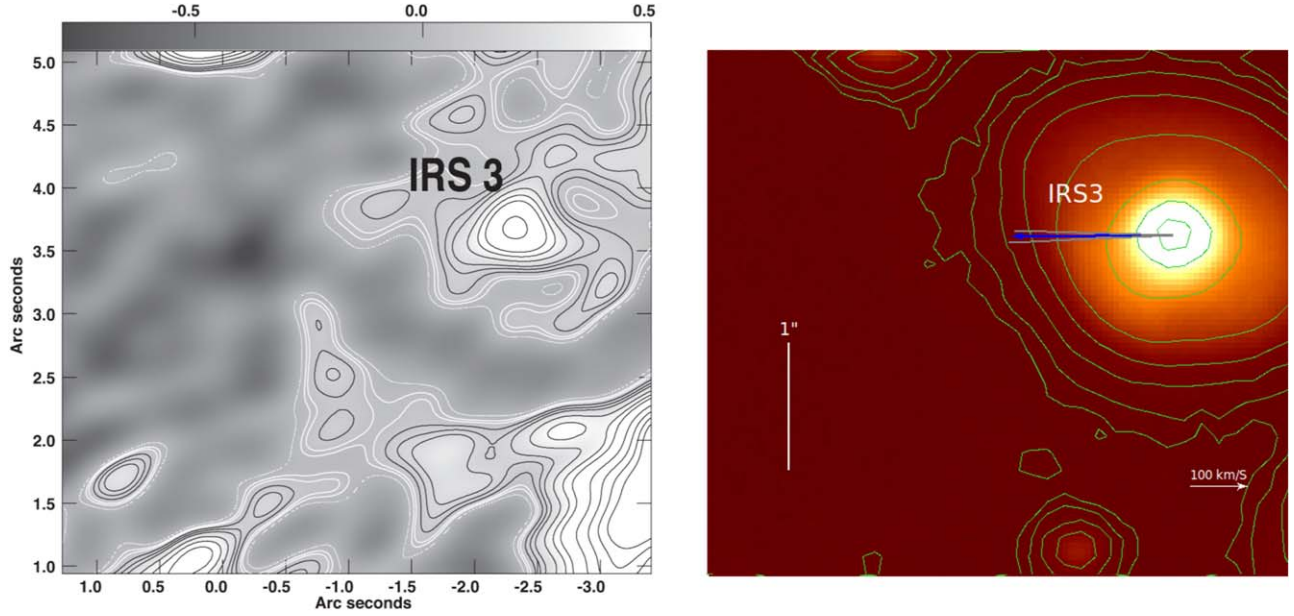


**Figure 9.** On the left is a 226 GHz emission of IRS 3 and its surroundings from Yusef-Zadeh et al. (2017) and on the right is an untreated PAH1 (8.6  $\mu\text{m}$ ) image.

- (a) Compression by the ram pressure produced by the collective stellar wind of the cluster of OB/WR stars within the NSC. For a simple estimate, we assume the mass range of the clumps to be  $m_{\text{clump}} \approx 10^{-2} - 10^{-4} M_{\odot}$ . We further assume an ambient number density of  $n_a \sim 10 \text{ cm}^{-3}$ , i.e., close to the Bondi-sphere value, and an outflow stellar wind velocity of  $v_w \sim 1000 \text{ km s}^{-1}$  (Najarro et al. 1997). For the stationary setup, in which the MIR filaments are pressure-confined by the wind pressure acting on the mini-spiral clumps moving with the orbital velocity of  $v_{\text{clump}} \sim 100 \text{ km s}^{-1}$  (Zhao et al. 2009), we can obtain their characteristic length scale using

$$\lambda_{\text{clump}} \sim \left( \frac{m_{\text{clump}} k_B T_{\text{clump}}}{\mu m_H [\mu m_H (v_{\text{clump}}^2 + v_w^2) - B^2/8\pi]} \right)^{1/3}, \quad (13)$$

where the ram pressure is balanced by the thermal pressure as well as the magnetic field inside the filaments. For a clump temperature of  $T_{\text{clump}} \sim 10^4 \text{ K}$  (Zhao et al. 2010) and a negligible magnetic field, the characteristic length scale is  $\lambda_{\text{clump}} \sim 10,500\text{--}2300 \text{ au}$ , which captures the range for the inferred length and the width of the MIR filaments; see Figure 10 (top-left panel). An aligned magnetic field in the northern arm (see, e.g., Aitken et al. 1998; Roche et al. 2018), has a tendency to increase the length scale of the clumps.

- (b) The blobs are the manifestation of the KH instability that arises due to the streaming motion of the mini-spiral in the surrounding hot plasma. This is especially the case for the northern and the eastern arms, which have more radial, elliptical orbits in comparison with the western arm (Zhao et al. 2009). For the estimate of the characteristic growth timescale of the KH instabilities of a certain size,  $\lambda_{\text{clump}} \sim 1000\text{--}10,000 \text{ au} \sim 1.5 \times 10^{16} - 1.5 \times 10^{17} \text{ cm}$ , we will assume a shearing velocity given by the terminal stellar wind velocity that is approximately perpendicular to the mini-spiral orbital motion, i.e.,  $v_w \sim 1000 \text{ km s}^{-1}$  and  $v_{\text{mini}} \sim 100 \text{ km s}^{-1}$ , which gives  $v_{\text{shear}} \sim \sqrt{v_w^2 + v_{\text{mini}}^2} \sim 1000 \text{ km s}^{-1}$ . The density of the ionized component of the mini-spiral was inferred to be  $n_{\text{mini}} \sim 3 - 21 \times 10^4 \text{ cm}^{-3}$  (Zhao et al. 2010), which sets the ratio with respect to the

ambient hot plasma to  $r = n_a/n_{\text{mini}} \sim 4.8 \times 10^{-5} - 3.3 \times 10^{-4}$ , assuming  $n_a \sim 10 \text{ cm}^{-3}$ . Using Equation (7), we get a KH growth timescale of  $\tau_{\text{KH}}(1000 \text{ au}) \sim 262\text{--}686 \text{ yr}$  and  $\tau_{\text{KH}}(10,000 \text{ au}) \sim 2620\text{--}6860 \text{ yr}$ . Since the lifetime of the mini-spiral is  $\sim 6 \times 10^4 \text{ yr}$ , as given by the mean orbital timescale of the arms (Zhao et al. 2009), the clumps of  $\lambda_{\text{clump}} \sim 1000 \text{ au}$  are continually forming as well as disappearing along the arms since their lifetime is comparable to the formation time as given by the evaporation timescale, see Equation (8), which gives  $\tau_{\text{evap}} \sim 480\text{--}3360 \text{ yr}$  for the clump size of  $\lambda_{\text{clump}} \sim 1000 \text{ au}$ , the density range of  $n_{\text{clump}} \sim 3 - 21 \times 10^4 \text{ cm}^{-3}$ , and the conductivity of the hot medium  $\kappa_H \sim 1.9 \times 10^{11} T_7^{5/2} \text{ erg s}^{-1} \text{ K}^{-1} \text{ cm}^{-1}$ , where  $T_7$  is in units of  $10^7 \text{ K}$ . This is consistent with the early considerations of the transient nature of ionized clouds in Sgr A West; see Lacy et al. (1980).

- (c) The denser clumps could have formed as a result of thermal instability during past states of a higher activity of Sgr A\* when its bolometric luminosity reached  $\sim 10^{39}\text{--}10^{41} \text{ erg s}^{-1}$ . This was proposed by Różańska et al. (2014), who studied the conditions for the thermal instability in the mini-spiral region. They concluded that the thermal instability does not operate in the current low-luminous state of Sgr A\*, but during the past periods of enhanced activity the thermal instability likely operated up to  $\sim 1.4 \text{ pc}$  from Sgr A\*, which led to the formation of a two-phase medium. This increased the clumpiness of the mini-spiral by creating clumps of  $\sim 1\text{--}100$  Earth masses, i.e.,  $3 \times 10^{-6}\text{--}3 \times 10^{-4} M_{\odot}$ . Based on the mini-spiral clump mass estimate presented in Section 4, the thermal instability clump mass appears to be lower by at least two orders magnitude. In case the thermal instability operated a few hundred years ago and clumps with the radius of  $R_{\text{clump}} \sim 10^{14}\text{--}10^{15} \text{ cm}$  and the mass of  $m_{\text{clump}} \sim 3 \times 10^{-5} M_{\odot}$  formed, then the evaporation timescale according to Equation (8) is long enough ( $\sim 10^3\text{--}10^4 \text{ yr}$ ) so that they could in principle survive until nowadays. However, by including the mechanical heating of the NSC, Różańska et al. (2017) concluded that cold

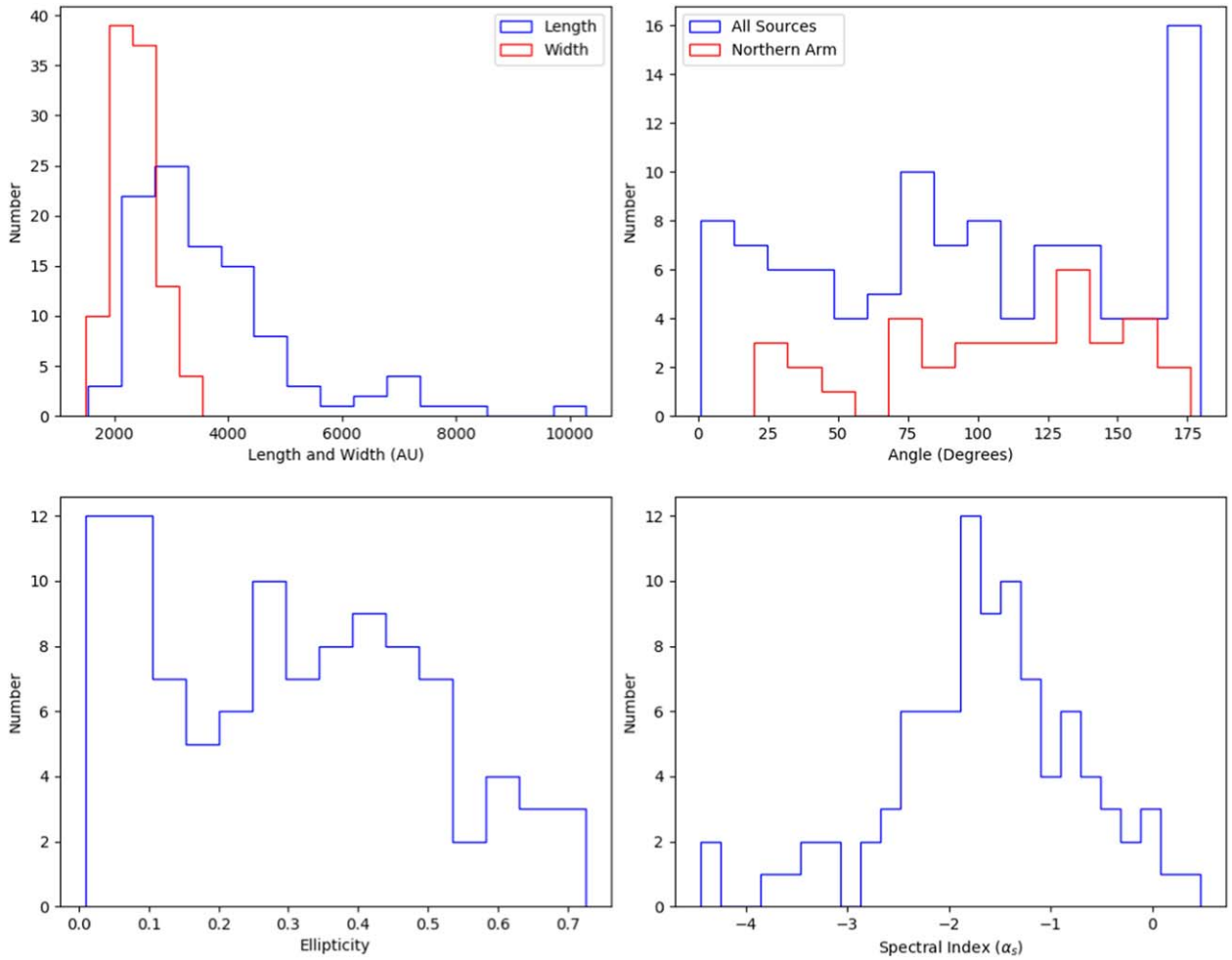


**Figure 10.** Histograms of the physical properties of the extended dusty sources. Most sources are about 3500–4000 au long and 2000 – 2500 au wide. Most sources are elliptic with various position angles. The sources on the northern arm seem to have a relatively tight spread of position angles compared to the rest of the sources.

clumps are not expected to form in the vicinity of Sgr A\* since stellar winds induce an outflow of the hot ambient plasma. This fact, in combination with the small clump mass, renders the instability scenario less plausible to explain the formation of the elongated MIR sources, unless each MIR filament would consist of at least 100 clumps formed via the thermal instability. However, since the models of Rózańska et al. (2014) and Rózańska et al. (2017) assume a spherical symmetry it is difficult to explain the filamentary structure of the instability clumps in this framework.

Regardless of the way the denser and brighter MIR clumps formed, their shape and orientation are the result of tidal prolongation along the streaming motion of the northern arm. This stems from the tidal radius estimated for a mini-spiral clump of radius  $R_{\text{clump}} \gtrsim 1000$  au and mass  $m_{\text{clump}} \leq 0.1 M_{\odot}$ :

$$\begin{aligned}
 r_t &\simeq R_{\text{clump}} \left( \frac{2M_{\bullet}}{m_{\text{clump}}} \right)^{1/3} \\
 &\sim 2.1 \left( \frac{R_{\text{clump}}}{1000 \text{ au}} \right) \left( \frac{m_{\text{clump}}}{0.1 M_{\odot}} \right)^{-1/3} \left( \frac{M_{\bullet}}{4 \times 10^6 M_{\odot}} \right)^{1/3} \text{ pc}.
 \end{aligned}
 \tag{14}$$

Since the mini-spiral arms are closer than 2 pc, any clump inside them is susceptible to tidal forces and prolongation parallel to the streaming (orbital) motion of the arms.

#### 4. Discussion

Here we present, to our knowledge, the largest consistent number of individual source identifications, proper motions, and thus tangential velocities, and MIR spectral indices in the central parsec of the galaxy, covering the central stellar cluster and the immediate Sgr A\* SMBH region. The MIR sources can clearly be divided into two groups: one associated with the flow along the extended mini-spiral, and one associated with dust-enshrouded stars and infrared-excess sources of the central stellar cluster.

Based on the color–temperature map derived from 12.5 to 20.3  $\mu\text{m}$  maps by Cotera et al. (1999), the overall temperature in the mini-spiral is of the order of  $\sim 200$  K. We assume that this is a good estimate of, or at least a lower limit to, the temperatures of the infrared-excess sources within the mini-spiral. A more exact estimate of the temperatures has to await multifrequency MIR data at a high angular resolution, as will be obtained, for example, with the METIS instrument at the extremely large telescope (Brandl et al. 2021).

For the sources not associated with stars, we estimate their dust masses based on PAH1 and Ne II<sub>2</sub> flux densities. We use

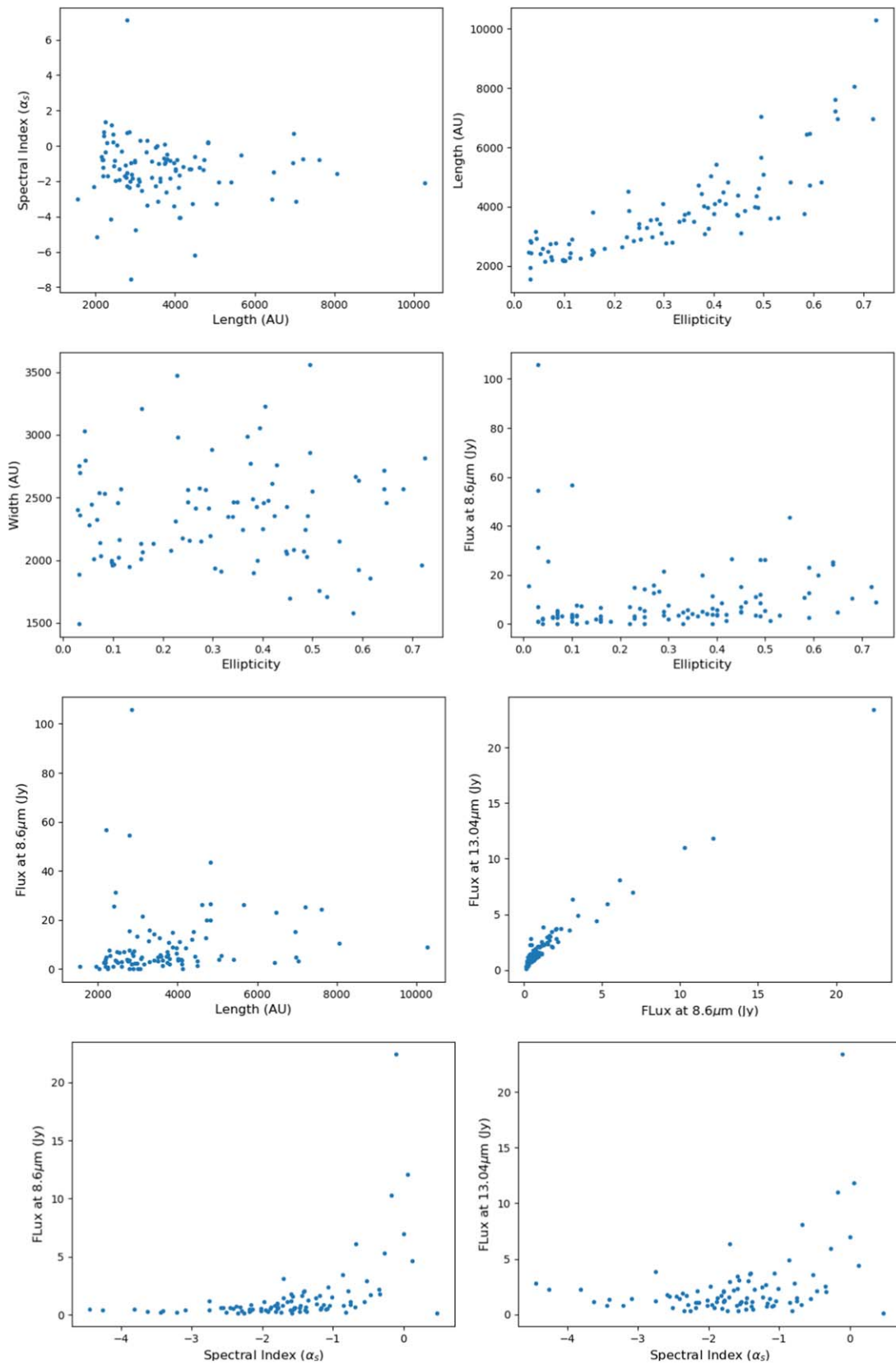


**Figure 11.** Correlation (or lack of it) among a few physical properties of the extended dusty sources. The spectral index ( $\alpha_s$ , using the convention  $F \propto \nu^{+\alpha_s}$ ) does not show a correlation with the length of the sources. Unsurprisingly, longer sources seem to be more elliptic. The flux densities at both the filters do correlate; however, the spectral index has a tighter correlation with flux at PAH1 than with flux at Ne II<sub>2</sub>. Although flux does not correlate with ellipticity or length, a few noticeable outliers are those associated with bright IRS sources.

**Table 4**  
Spearman Correlation Coefficients between Quantities that Characterize Compact MIR Dusty Sources

	Length	Width	Angle	Flux (PAH1)	Flux (Ne II <sub>2</sub> )	Spectral index	Ellipticity
Length	...	0.064 (0.524)	-0.098 (0.326)	0.260 (0.008)	0.404 ( $2.310 \times 10^{-5}$ )	-0.136 (0.171)	0.715 ( $2.04 \times 10^{-17}$ )
Width	0.064 (0.524)	...	-0.091(0.361)	0.146(0.140)	0.235(0.017)	-0.078(0.432)	0.048(0.630)
Angle	-0.098 (0.326)	-0.091(0.361)	...	-0.074(0.457)	-0.180(0.069)	0.089 (0.372)	-0.106(0.287)
Flux (PAH1)	0.260 (0.008)	0.146(0.140)	-0.074(0.457)	...	0.850( $7.36 \times 10^{-30}$ )	0.510( $3.65 \times 10^{-8}$ )	0.307(0.0016)
Flux (Ne II <sub>2</sub> )	0.404 ( $2.310 \times 10^{-5}$ )	0.235(0.017)	-0.180(0.069)	0.850( $7.36 \times 10^{-30}$ )	...	0.081(0.419)	0.382( $6.70 \times 10^{-5}$ )
Spectral Index	-0.136 (0.171)	-0.078(0.432)	0.089 (0.372)	0.510( $3.65 \times 10^{-8}$ )	0.081(0.419)	...	-0.073(0.466)
Ellipticity	0.715 ( $2.04 \times 10^{-17}$ )	0.048(0.630)	-0.106(0.287)	0.307(0.0016)	0.382( $6.70 \times 10^{-5}$ )	-0.073(0.466)	...

**Note.** In parentheses, we include the  $p$ -value. Five significant positive correlations were found: length flux (Ne II<sub>2</sub>), length–ellipticity, flux (PAH1)–flux (Ne II<sub>2</sub>), flux (PAH1)–spectral index, and flux (Ne II<sub>2</sub>)–ellipticity.



the relation based on Rieke et al. (1978) and Kunneriath et al. (2012),

$$M_d = \frac{F(\nu)D_{GC}^2}{B(\nu, T_d)} \frac{4a}{3Q(\nu)} \rho_d, \quad (15)$$

where  $F(\nu)$  is the measured flux density and  $B(\nu, T_d)$  is the Planck function calculated for a dust temperature of  $T_d \sim 200$  K (Cotera et al. 1999). The dust is characterized by the mean values of the radius,  $a = 0.1 \mu\text{m}$ , the mass density,  $\rho_d = 2 \text{ g cm}^{-3}$ , and the emissivity,  $Q \approx 10^{-3} - 10^{-2}$  close to  $10 \mu\text{m}$  (Aannestad 1975; Rieke et al. 1978). The distance to the GC is set to  $D_{GC} = 8.1$  kpc. Assuming a gas-to-dust ratio of  $\sim 100$ , we obtain a mean gas mass of the mini-spiral clump,  $\bar{M}_g(\text{PAH1}) \sim 0.046 - 0.46 M_\odot$  and  $\bar{M}_g(\text{Ne ii}_2) \sim 0.015 - 0.15 M_\odot$ , as based on 85 dusty filaments that are not associated with stellar sources. These values are consistent within a factor of 3. Considering the peak width of the clumps,  $w \sim 2000$  au, and the peak length,  $l \sim 3000$  au, we obtain the characteristic clump volume of  $V_{\text{clump}} \sim 3.2 \times 10^{49} \text{ cm}^3$ , which yields a filament number density in the range of  $n_{\text{clump}} \sim 1.1 \times 10^6 - 3.4 \times 10^7 \text{ cm}^{-3}$ , which is at least one order of magnitude more than the electron number density of the ionized component,  $n_e = (3-21) \times 10^4 \text{ cm}^{-3}$  (Zhao et al. 2010). The filaments could thus be overdense regions that are either pressure-confined by the stellar winds of OB/WR stars or they could stand for KH instabilities that got denser due to radiative cooling. This supports the multiphase nature of the mini-spiral streamers, with denser filaments embedded within a more diluted ionized gas (Różańska et al. 2014). Denser dusty filaments could also be the sites of the water- and CO-ice features and hydrocarbons detected within the central parsec (Moultaka et al. 2015a, 2015b). If the mean clump gas mass is in the range of  $\sim 0.01 - 0.1 M_\odot$  and we have  $\sim 100$  filaments, then their total gas mass of  $\sim 1 - 10 M_\odot$  is consistent with the total ionized gas mass of  $\sim 60 M_\odot$  within the central cavity (Lo & Claussen 1983). The denser filaments are currently not massive and dense enough to form stellar and substellar objects. As discussed in the previous section, they are transient features formed via the KH instability along the streaming motion and they evaporate on a timescale of  $\sim 100 - 1000$  yr. The filaments are also expected to be tidally elongated along the streaming motion of the mini-spiral during their lifetime.

Mužić et al. (2007) show that the shape and motion of the mini-spiral filaments do not agree with a purely Keplerian motion of gas in the potential of the SMBH at the position of Sgr A\*. The authors involve additional mechanisms that are responsible for the formation and the motion of these filaments. They assume that the filaments are affected by an outflow from the disk of young mass-losing stars around Sgr A\*. In addition, an outflow from the Sgr A\* black hole region itself may be responsible for the elongated shape and the motion of the filaments.

## 5. Summary

We studied MIR images of the central parsec of the GC in the  $N$  band (8.6 and  $13.04 \mu\text{m}$ ). As the MIR emission is dominated by dust and extended regions around the central SMBH, we applied a high-pass filter on the images to resolve and identify the sources. We present the proper motions of these extended objects over a 12 yr time period. There are two distinct types of the observed motion: one related to infrared-excess sources of the central stellar cluster and the other a stream-like motion of extended objects along the mini-spiral streamer. We also present the flux densities of all the sources using elliptical apertures. Using the spectral indices, we infer that the MIR region is dominated by dust-enshrouded stars or colder dusty filaments and the temperature of  $\sim 200$  K (Cotera et al. 1999) is at least the lower limit of infrared-excess sources within the mini-spiral. We detect a bow-shock feature and tail components of IRS 7 that are pointed away from Sgr A\*. The proper-motion distribution of the individual tail components can be interpreted with a combination of downstream fluid motion and the development of KH instabilities. We detect and resolve the brightest MIR source in the region, IRS 3. The extended structure of the star is likely a result of its atmosphere's perturbation followed by tidal prolongation. We also report on the nature of all the dusty sources and delve into their possible origins.

This work was supported in part by SFB 956, ‘‘Conditions and Impact of Star Formation.’’ H.B. and E.H. are members of the International Max Planck Research School for Astronomy and Astrophysics at the Universities of Bonn and Cologne. We thank the Collaborative Research Centre 956, subproject A02, funded by the Deutsche Forschungsgemeinschaft (DFG), project ID 184018867. N.B.S. acknowledges financial support from the Austrian National Science Foundation through a FWF standalone grant No. P31154-N27. M.Z. acknowledges financial support by the GAČR EXPRO grant No. 21-13491X, ‘‘Exploring the Hot Universe and Understanding Cosmic Feedback.’’ R.S. acknowledges financial support from the State Agency for Research of the Spanish MCIU through the ‘‘Center of Excellence Severo Ochoa’’ award for the Instituto de Astrofísica de Andalucía (grant No. SEV-2017-0709) and financial support from national project PGC2018-095049-B-C21 (MCIU/AEI/FEDER, UE).

## Appendix A

### Tangential Velocity Comparisons between MIR and $K$ -band Velocities

A comparison between the  $K$ -band tangential velocity (Schödel et al. 2009; Genzel et al. 2000) and our MIR velocities for the point sources (see Table 5) looks favorable. The mean absolute difference of around  $\pm 100 \text{ km s}^{-1}$  is most likely affected by the larger PSF in the MIR, the limited baseline in time, and the fact that even the point sources may show some IR excess/extension or they are located on background emission that is spatially structured/variable on the scales of the PSF. Figures 12 and 13 in depict the deviations from Schödel et al. (2009).

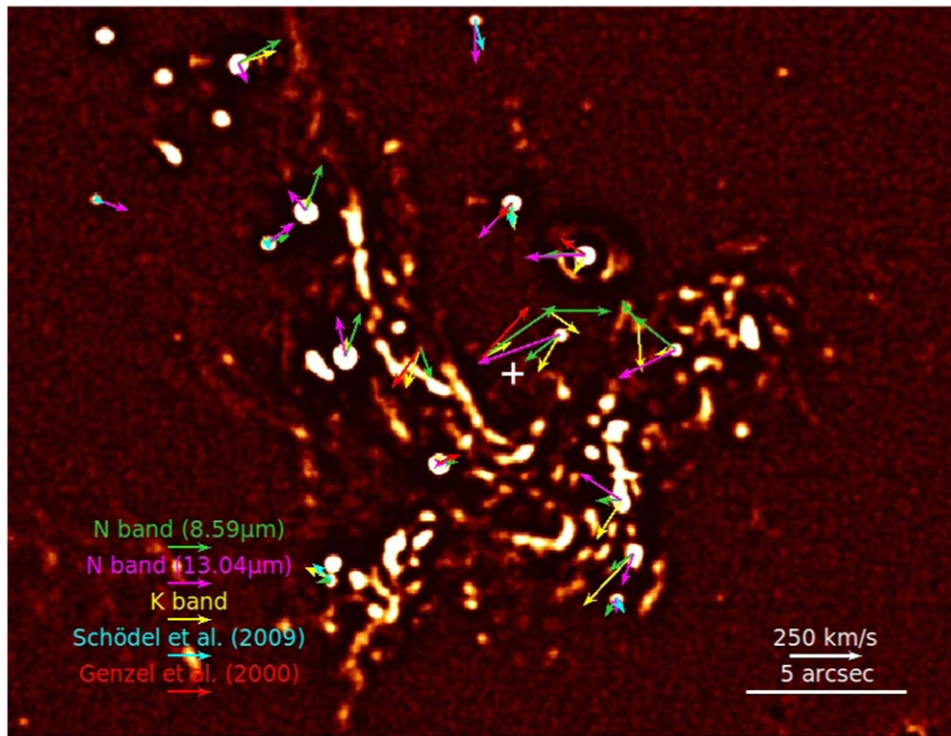


**Figure 12.** Comparison velocities from the *K* band and from Schödel et al. (2009) and Genzel et al. (2000).

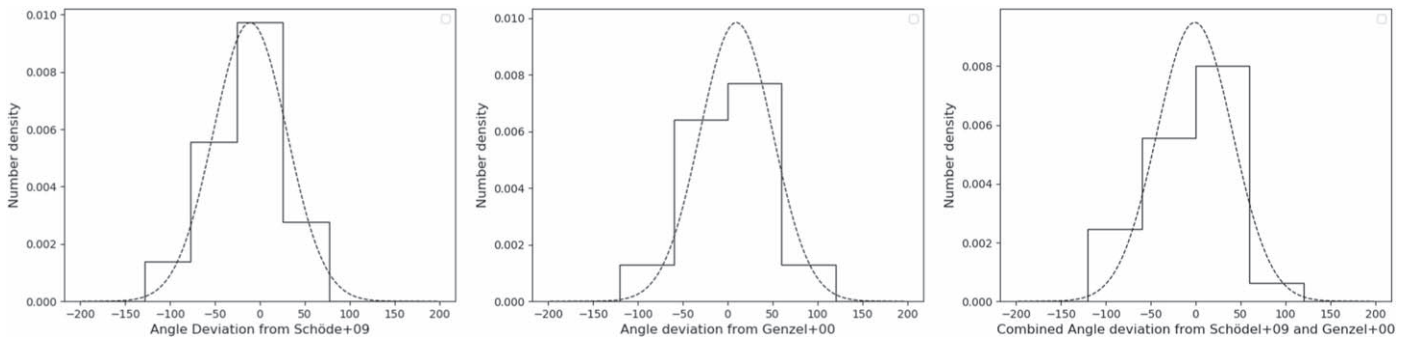


**Figure 13.** Angle deviations from Schödel et al. (2009) and Genzel et al. (2000) values in all the wavelengths. Mean absolute deviation in velocity (R.A.) is about  $102 \text{ km s}^{-1}$ , in velocity (decl.) is about  $76 \text{ km s}^{-1}$ , and the standard deviation of the angle difference is about  $40^\circ$ .

**Table 5**  
Comparison of Stellar Tangential Velocities in PAH1 and Ne II<sub>2</sub> Bands with those in the K Band

Source	PAH1		Ne II		K			S09				G00				
	$v_\alpha$	$v_\delta$	$v_\alpha$	$v_\delta$	$v_\alpha$	$\Delta v_\alpha$	$v_\delta$	$\Delta v_\delta$	$v_\alpha$	$\Delta v_\alpha$	$v_\delta$	$\Delta v_\delta$	$v_\alpha$	$\Delta v_\alpha$	$v_\delta$	$\Delta v_\delta$
IRS 5	-303	167	-71	-145	-267	6	84	12								
IRS 10W	-118	331	120	148	-29	6	115	10								
IRS 10EE*	-157	54	-186	142	-44	6	-16	10	-15	7	-60	7				
IRS 1W	-113	307	53	275	-9	6	131	10								
IRS 16NE	-83	-224			104	6	-281	10					199	65	-279	21
IRS 16C	-513	358			-211	6	108	10					-330	39	353	34
IRS 21	-138	8	-65	3	-1	6	-43	10					-159	65	64	38
IRS 9*	97	-22			176	6	90	10	127	10	116	10				
IRS 2S	180	-124	82	-230	352	8	-368	14								
IRS 2L	173	-2	293	191	174	8	-273	10								
IRS 29	256	-186	585	-205	165	6	-261	10								
IRS 29NE	-435	7			-215	6	-151	10								
IRS 34	119	166			-24	8	-335	10								
IRS 6E	294	234	398	-206	141	6	-39	10								
IRS 3	282	-2	412	-13	84	8	-137	10					170	40	115	45
IRS 7*	27	-125	232	-250	-23	8	-193	12	-2	9	-176	9	100	67	-118	35
IRS 12N*	80	-133	-5	-106					-62	8	-107	8				
IRS 15NE*	-67	-133	-6	-308					-58	6	-223	6				
IRS 17*	-351	198	-238	-83					-65	5	-40	5				

**Note.** All velocities are in kilometers per second. S09 is the data from Schödel et al. (2009). G00 is the data from Genzel et al. (2000). Sources used as calibrators are marked with \*. We chose a conservative 0.25 pixel uncertainty for PAH1 and Ne II<sub>2</sub> proper motions, which corresponds to about 45 km s<sup>-1</sup>.

## Appendix B

### N-band Flux Density Comparison









Table 6 presents a comparison of our measured flux densities with Viehmann et al. (2006), using both circular apertures and elliptic apertures determined by their FWHM.

**Table 6**  
Comparison of Measured Flux Densities (Reddened) with *N*-band Fluxes of Viehmann et al. (2006)

Source	F (Jy) (V+06)	PAH1 F (Jy) (Circular)	F (Jy) (FWHM)	±F (Jy)	F (Jy) (V+06)	Ne II_2 F (Jy) (Circular)	F (Jy) (FWHM)	±F (Jy)
IRS 5NE*	0.51	0.59	0.57	0.09	0.56	0.50	1.00	0.09
IRS 5E	0.59	0.38	0.49	0.08	1.54	0.57	1.99	0.17
IRS 5S	0.63	0.25	0.61	0.09	0.38	0.29	2.35	0.20
IRS 5	5.11	5.44	3.92	0.60	5.85	4.78	4.54	0.38
IRS 10W*	11.06	10.18	8.33	1.27	11.85	10.94	11.61	0.98
IRS 7*	1.47	1.26	1.15	0.18	1.75	1.95	2.04	0.17
IRS 3	13.42	16.35	8.65	1.31	12.85	11.17	11.75	0.99
IRS 1W*	20.42	22.96	16.14	2.45	22.93	25.40	21.97	1.85
IRS 21	4.56	4.95	4.79	0.73	5.44	6.27	6.92	0.58
IRS 29	0.15	0.07	0.13	0.02				
IRS 2L	5.26	4.25	3.28	0.50	7.49	6.45	5.52	0.47
IRS 9	0.21	0.58	0.39	0.06				

**Note.** Uncertainties in V + 06 flux densities are ±30%. Sources used as flux calibrators are marked with \*.

### ORCID iDs

Harshitha K. Bhat  <https://orcid.org/0000-0002-4408-0650>  
 Nadeen B. Sabha  <https://orcid.org/0000-0001-7134-9005>  
 Michal Zajaček  <https://orcid.org/0000-0001-6450-1187>  
 Andreas Eckart  <https://orcid.org/0000-0001-6049-3132>  
 Rainer Schödel  <https://orcid.org/0000-0001-5404-797X>  
 S. Elaheh Hosseini  <https://orcid.org/0000-0002-3004-6208>  
 Florian Peißker  <https://orcid.org/0000-0002-9850-2708>  
 Anton Zensus  <https://orcid.org/0000-0001-7470-3321>

### References

- Aannestad, P. A. 1975, *ApJ*, **200**, 30  
 Aitken, D. K., Smith, C. H., Moore, T. J. T., & Roche, P. F. 1998, *MNRAS*, **299**, 743  
 Baganoff, F. K., Maeda, Y., Morris, M., et al. 2003, *ApJ*, **591**, 891  
 Becklin, E. E., Gatley, I., & Werner, M. W. 1982, *ApJ*, **258**, 135  
 Blandford, R. D., & Begelman, M. C. 1999, *MNRAS*, **303**, L1  
 Blank, M., Morris, M. R., Frank, A., Carroll-Nellenback, J. J., & Duschl, W. J. 2016, *MNRAS*, **459**, 1721  
 Blum, R. D., Sellgren, K., & Depoy, D. L. 1996, *ApJ*, **470**, 864  
 Borkar, A., Eckart, A., Straubmeier, C., et al. 2020, in *Multifrequency Behaviour of High Energy Cosmic Sources (Trieste: SISSA)*, 33  
 Bower, G. C., Wright, M. C. H., Falcke, H., & Backer, D. C. 2003, *ApJ*, **588**, 331  
 Brandl, B., Bettonvil, F., van Boekel, R., et al. 2021, *Msngr*, **182**, 22  
 Carr, J. S., Sellgren, K., & Balachandran, S. C. 2000, *ApJ*, **530**, 307  
 Christopher, M. H., Scoville, N. Z., Stolovy, S. R., & Yun, M. S. 2005, *ApJ*, **622**, 346  
 Cotera, A., Morris, M., Ghez, A. M., et al. 1999, in *ASP Conf. Ser. 186, The Central Parsecs of the Galaxy*, ed. H. Falcke et al. (San Francisco, CA: ASP), 240  
 Cowie, L. L., & McKee, C. F. 1977, *ApJ*, **211**, 135  
 Eckart, A., Genzel, R., Krabbe, A., et al. 1992, *Natur*, **355**, 526  
 Eckart, A., Genzel, R., Ott, T., & Schödel, R. 2002, *MNRAS*, **331**, 917  
 Eckart, A., Hüttemann, A., Kiefer, C., et al. 2017, *FoPh*, **47**, 553  
 Falcke, H., & Markoff, S. B. 2013, *CQGra*, **30**, 244003  
 Fritz, T. K., Gillessen, S., Dodds-Eden, K., et al. 2011, *ApJ*, **737**, 73  
 Genzel, R., Eisenhauer, F., & Gillessen, S. 2010, *RvMP*, **82**, 3121  
 Genzel, R., Pichon, C., Eckart, A., Gerhard, O. E., & Ott, T. 2000, *MNRAS*, **317**, 348  
 Gravity Collaboration, Rodríguez-Coira, G., Paumard, T., et al. 2021, *A&A*, **651**, A37  
 Hsieh, P.-Y., Koch, P. M., Kim, W.-T., et al. 2021, *ApJ*, **913**, 94  
 Jackson, J. M., Geis, N., Genzel, R., et al. 1993, *ApJ*, **402**, 173  
 Karas, V., Svoboda, J., & Zajaček, M. 2021, arXiv:1901.06507  
 Kunneriath, D., Eckart, A., Vogel, S. N., et al. 2012, *A&A*, **538**, A127  
 Lacy, J. H., Townes, C. H., Geballe, T. R., & Hollenbach, D. J. 1980, *ApJ*, **241**, 132  
 Lo, K. Y., & Claussen, M. J. 1983, *Natur*, **306**, 647  
 Lutz, D., Krabbe, A., & Genzel, R. 1993, *ApJ*, **418**, 244  
 Marrone, D. P., Moran, J. M., Zhao, J.-H., & Rao, R. 2006, *ApJ*, **640**, 308  
 Mills, E. A. C., Güsten, R., Requena-Torres, M. A., & Morris, M. R. 2013, *ApJ*, **779**, 47  
 Mossoux, E., & Eckart, A. 2018, *MNRAS*, **474**, 3787  
 Moultaqa, J., Eckart, A., & Mužić, K. 2015a, *ApJ*, **806**, 202  
 Moultaqa, J., Eckart, A., & Sabha, N. 2015b, *MNRAS*, **448**, 3363  
 Moultaqa, J., Eckart, A., Viehmann, T., et al. 2004, *A&A*, **425**, 529  
 Mužić, K., Eckart, A., Schödel, R., et al. 2010, *A&A*, **521**, A13  
 Mužić, K., Eckart, A., Schödel, R., Meyer, L., & Zensus, A. 2007, *A&A*, **469**, 993  
 Najarro, F., Krabbe, A., Genzel, R., et al. 1997, *A&A*, **325**, 700  
 Nitschai, M. S., Neumayer, N., & Feldmeier-Krause, A. 2020, *ApJ*, **896**, 68  
 Ott, T. 2012, QFitsView: FITS file viewer, Astrophysics Source Code Library, ascl:1210.019  
 Ott, T., Eckart, A., & Genzel, R. 1999, *ApJ*, **523**, 248  
 Paumard, T., Genzel, R., Martins, F., et al. 2006, *ApJ*, **643**, 1011  
 Paumard, T., Pfuhl, O., Martins, F., et al. 2014, *A&A*, **568**, A85  
 Peißker, F., Ali, B., Zajaček, M., et al. 2021, *ApJ*, **909**, 62  
 Peißker, F., Eckart, A., Sabha, N. B., Zajaček, M., & Bhat, H. 2020a, *ApJ*, **897**, 28  
 Peißker, F., Hosseini, S. E., Zajaček, M., et al. 2020b, *A&A*, **634**, A35  
 Peißker, F., Zajaček, M., Eckart, A., et al. 2019, *A&A*, **624**, A97  
 Reid, M. J., Menten, K. M., Genzel, R., et al. 2003, *ApJ*, **587**, 208  
 Rieke, G. H., Telesco, C. M., & Harper, D. A. 1978, *ApJ*, **220**, 556  
 Rózańska, A., Czerny, B., Kunneriath, D., et al. 2014, *MNRAS*, **445**, 4385  
 Rózańska, A., Kunneriath, D., Czerny, B., Adhikari, T. P., & Karas, V. 2017, *MNRAS*, **464**, 2090  
 Roche, P. F., Lopez-Rodriguez, E., Telesco, C. M., Schödel, R., & Packham, C. 2018, *MNRAS*, **476**, 235  
 Schödel, R., Eckart, A., Alexander, T., et al. 2007, *A&A*, **469**, 125  
 Schödel, R., Feldmeier, A., Neumayer, N., Meyer, L., & Yelda, S. 2014, *CQGra*, **31**, 244007  
 Schödel, R., Merritt, D., & Eckart, A. 2009, *A&A*, **502**, 91  
 Serabyn, E., Lacy, J. H., & Achtermann, J. M. 1991, *ApJ*, **378**, 557  
 Shukla, H., Yun, M. S., & Scoville, N. Z. 2004, *ApJ*, **616**, 231  
 Stolovy, S. R., Hayward, T. L., & Herter, T. 1996, *ApJL*, **470**, L45  
 Tanner, A., Ghez, A. M., Morris, M., et al. 2002, *ApJ*, **575**, 860  
 Tsuboi, M., Kitamura, Y., Tsutsumi, T., et al. 2020, *PASJ*, **72**, 36  
 Viehmann, T., Eckart, A., Schödel, R., et al. 2005, *A&A*, **433**, 117  
 Viehmann, T., Eckart, A., Schödel, R., Pott, J. U., & Moultaqa, J. 2006, *ApJ*, **642**, 861  
 Vollmer, B., Beckert, T., & Duschl, W. J. 2004, *A&A*, **413**, 949  
 Vollmer, B., & Duschl, W. J. 2000, *NewA*, **4**, 581  
 Wang, Q. D., Nowak, M. A., Markoff, S. B., et al. 2013, *Sci*, **341**, 981

Yusef-Zadeh, F., & Melia, F. 1992, [ApJL](#), **385**, L41  
Yusef-Zadeh, F., & Morris, M. 1991, [ApJL](#), **371**, L59  
Yusef-Zadeh, F., Morris, M., & Ekers, R. D. 1990, [Natur](#), **348**, 45  
Yusef-Zadeh, F., Royster, M., Wardle, M., et al. 2020, [MNRAS](#), **499**, 3909  
Yusef-Zadeh, F., Wardle, M., Cotton, W., et al. 2017, [ApJ](#), **837**, 93

Zajaček, M., Araudo, A., Karas, V., et al. 2020b, arXiv:2011.12868  
Zajaček, M., Araudo, A., Karas, V., Czerny, B., & Eckart, A. 2020a, [ApJ](#), **903**, 140  
Zhao, J.-H., Blundell, R., Moran, J. M., et al. 2010, [ApJ](#), **723**, 1097  
Zhao, J.-H., Morris, M. R., Goss, W. M., & An, T. 2009, [ApJ](#), **699**, 186